
Angular analysis of the decay $B^0 \rightarrow K^{*0} J/\psi (\rightarrow e^+ e^-)$

MASTER THESIS

Bas Hofman BSc.

Supervisors:

dr. Wouter Hulsbergen
NIKHEF

dr. Miriam Lucio Martínez
NIKHEF

Second examiner:

Prof. dr. Raimond Snellings
Utrecht University

4 September 2020

Abstract

In this thesis the angular analysis of the $B^0 \rightarrow K^{*0} J/\psi (\rightarrow e^+ e^-)$ decay is presented. This decay serves as a control channel in the decay $B^0 \rightarrow K^{*0} e^+ e^-$. The angular observables describing the angular distributions of the decay were determined from a fit. The data sample that was used in this analysis is the data gathered by the LHCb detector in the year 2016 and corresponds to an integrated luminosity of 1.665 fb^{-1} at a total centre-of-momentum energy of 13 TeV. The S-wave component from the $K^+ \pi^-$ system was included in the PDF describing the angular distributions. This contribution accounted for $\sim 12\%$ of the events. The results from this analysis are statistically incompatible with the results of the angular analysis of $K^{*0} J/\psi (\rightarrow \mu^+ \mu^-)$. However, a more extensive study of the various background components and their angular behaviour is needed.

Contents

1	Introduction	1
1.1	The Standard Model	1
1.1.1	Why go beyond the Standard Model?	2
1.2	Lepton Universality	2
1.3	Semileptonic B meson decays	3
1.3.1	Angular analysis of the decay $B^0 \rightarrow K^{*0} \ell \bar{\ell}$	5
2	Detector	6
2.1	Magnet	7
2.2	Tracking	7
2.2.1	VERTex LOCator (VELO)	8
2.2.2	Tracker Turicensis (TT)	8
2.2.3	Inner Tracker (IT)	9
2.2.4	Outer Tracker (OT)	9
2.3	Particle identification	10
2.3.1	RICH	10
2.3.2	Calorimeter	11
2.3.3	Muon system	11
2.3.4	Final PID	12
2.4	Trigger	12
3	Analysis Strategy	14
3.1	Definition of decay angles	14
3.2	Angular PDF	16
3.3	Acceptance	18
3.3.1	Normalisation	19
3.3.2	Acceptance projections	19
4	Data and Selection	21
4.1	Stripping	21
4.2	Trigger	21
4.3	Preselection	23
4.3.1	B mass, q^2 window and other kinematic cuts	24
4.3.2	Particle Identification cuts	25
4.3.3	Boosted Decision Tree	25
4.4	sWeights	27
4.4.1	sPlot technique	27
4.4.2	Implementation of sWeights	28
5	Fit Framework	32
5.1	Validating the Fitter	32
5.1.1	Extracting the PDF parameters	32
5.1.2	Fitting generator level Monte Carlo	33
5.1.3	Pseudo-experiments	34
5.1.4	Fitting reconstructed Monte Carlo	36
6	Results	38

1 Introduction

1.1 The Standard Model

In particle physics the Standard Model (SM) is the theory describing three of the fundamental forces governing the interaction of matter. The forces that are described by the SM are the electromagnetic force, the weak force and the strong force. Gravity is not included in the Standard Model. Each force in the SM had associated quantum numbers that dictate the coupling strength of the relevant force.

The particles in the SM are classified in two main groups: fermions and bosons. The bosons are the force carrier particles in the Standard Model. The fermion group consists of two further classes, namely the quarks and the leptons. Quarks have a non-zero charge for the strong force, and are the particles that make up matter like protons and neutrons. Leptons are spin 1/2 particles that do not interact strongly, their relevant quantum number for colour is zero. Leptons do however interact via the weak, and if they are charged, electromagnetic forces. The best known member of the lepton class is the electron.

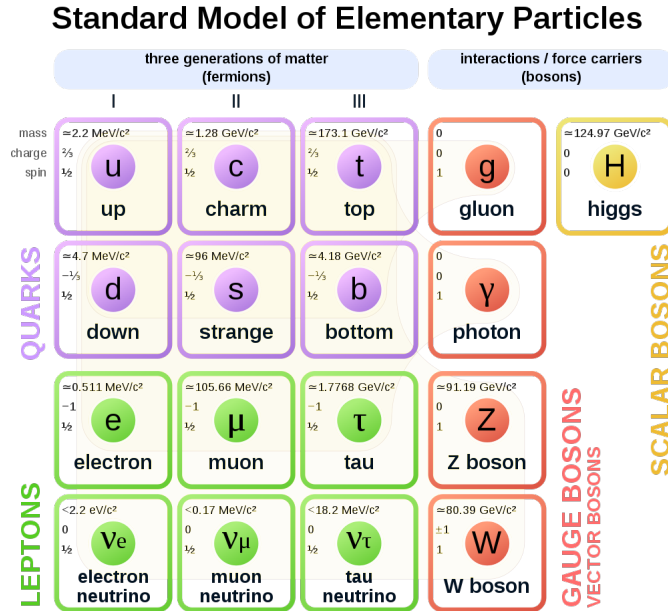


Figure 2: The particles of the Standard Model grouped by their classes.

The leptons in the SM are categorized in three generations, with each generation consisting of two particles adding up to a total of six particles. The two particles within one generation are the charged lepton and its lepton neutrino. All six particles come with corresponding antiparticles. Within the Standard Model these lepton generations only differ by their mass. That means that the force carrier particles, the photon, the W boson and the Z boson, couple equally strong to these generations. This property of the Standard Model has been tested extensively. The name of this property is Lepton Universality (LU). If a violation of this effect is found, it would be a clear indication of physics beyond the Standard Model.

1.1.1 Why go beyond the Standard Model?

While the Standard Model (SM) is a very robust theory, it is not a ‘Theory of Everything’. Apart from the fact that gravity is not described by the Standard Model, there are more things it cannot explain. One example is the baryon asymmetry observed in the universe, which cannot be accommodated within the context of the SM. Searches for physics beyond the Standard Model, or New Physics (NP), are therefore a very interesting area of research.

At the Large Hadron Collider (LHC) signatures of New Physics are actively being searched for. One of the ways in which this is done is by looking for new particles that might have been created in the detector. The high energy of the LHC allows it to probe energy ranges not accessible by previous accelerators. However, it is also possible to look for signs of New Physics by means of precision measurements.

The main advantage of this high precision type of measurement is that such high energies are no longer needed, as particles are not directly detected but rather influence the underlying physics process via loop diagrams. That means that the high mass particle does not need to end up in the final state for it to influence the measurement. In that case the intermediate particle is called a virtual particle. A good example of this is the history leading up to the discovery of the top quark [1]. Before the top quark was directly detected bounds on its mass were set by measuring the masses and couplings of the W and Z bosons.

1.2 Lepton Universality

In the Standard Model all three lepton generations have the same quantum numbers. This makes them couple to gauge bosons equally strong over all generations. The difference between the generations stem from their Yukawa coupling to the Higgs field. This gives each generation a different mass. When we diagonalise the Yukawa matrix for the fermions, we find that the weak eigenstates no longer correspond one to one to the mass eigenstates imposed by the Higgs symmetry breaking. This is similar to the behaviour in the quark sector of the Standard Model where the Cabibbo–Kobayashi–Maskawa matrix is a matrix that gives the relation of the weak quark eigenstates with the quark mass eigenstates. For the leptons a similar mixing matrix is introduced. This matrix is called the PMNS matrix for Pontecorvo–Maki–Nakagawa–Sakata and is graphically represented in figure 3.

When studying the possible violation of Lepton Universality it is important to consider the effects the CKM and PMNS matrices will have on the observables. Most of the values of the matrix elements of the CKM and PMNS matrices carry relatively high uncertainties with them [3]. Also the bound states of the involved hadrons can not be described perturbatively. This will impact the precision of the analysis. Therefore it is desirable if to minimise the effect these matrix elements have on the analysis precision. With Flavour Changing Neutral Current transitions, where an up-type quark transitions into a different up-type quark, we can not determine from the initial and final state particles which CKM element was relevant for the interaction, as we do not know what quark flavour propagated in the loop. However, due to the strong hierarchy within the CKM matrix we can determine a leading term for the interaction.

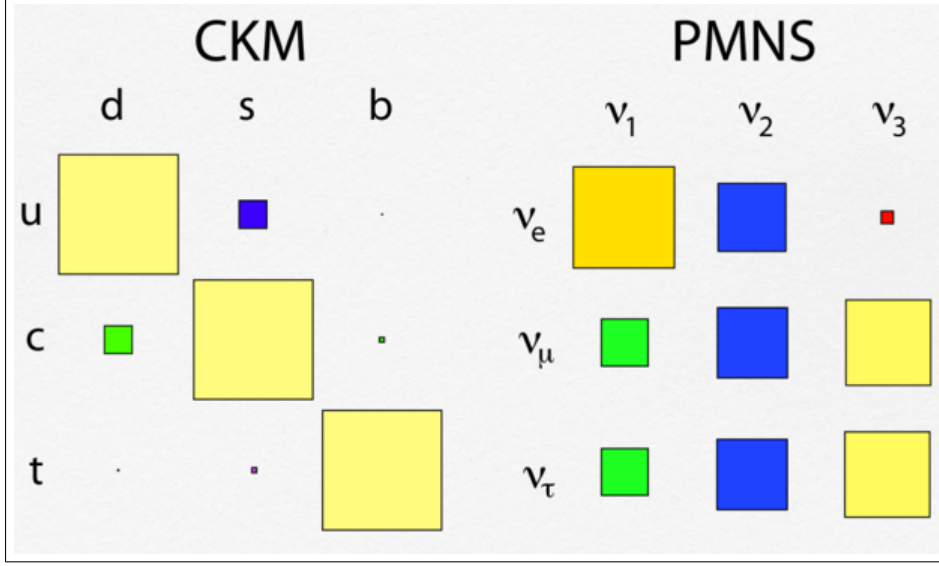


Figure 3: Graphic illustration of the CKM (left) and PMNS (right) matrices. These CKM and PMNS matrices give the mixing between the weak and mass eigenstates for quarks and leptons respectively. The size of each box reflects the value of the matrix element [2].

A good way to handle the uncertainty that comes with the CKM and PMNS matrix elements is the utilisation of ratios between transitions. When we want to test Lepton Universality in the decay of beauty quarks it makes sense to take the ratio of two transitions that only differ in their lepton content and not in their quark content. In that way the relevant CKM matrix element, and QCD effects describing the bound state of quarks, cancel out of the ratio. An example would be the ratio between decays containing the $b \rightarrow c\tau^-\bar{\nu}_\tau$ transition and decays containing the $b \rightarrow c\mu^-\bar{\nu}_\mu$ transition. In this case the CKM element V_{cb} , and the QCD effects describing the bound states of the quarks will drop out.

1.3 Semileptonic B meson decays

Mesons are particles that consist of two quarks, with B mesons containing a b quark. If they decay to a final state that consists of both leptons and hadrons it is called a semileptonic decay. Such decays of B mesons can serve as a stringent test on Lepton Universality. This thesis will focus on the decay of a B meson with a Kaon in the final state. Bottom quarks can decay into strange quarks by emission of two charged leptons, $b \rightarrow s\ell^-\ell^+$. This type of decay does not occur at the tree level within the SM and is mediated by a Flavour Changing Neutral Current (FCNC), which makes them very suppressed. Examples of decays of this type are $B^{+(0)} \rightarrow K^{+(0)}\ell^+\ell^-$ and $B^{+(0)} \rightarrow K^{*+(0)}\ell^+\ell^-$ where ℓ is either an electron or a muon. Within the SM, the decay $B^0 \rightarrow K^{*0}\ell^+\ell^-$ is mediated by electroweak box and loop diagrams that are shown in figure 4. The K^{*0} particle represents the $K^{*0}(892)$ resonance that is reconstructed as $K^{*0} \rightarrow K^+\pi^-$. The relative contribution of these diagrams is dependant on the invariant mass of the dilepton pair.

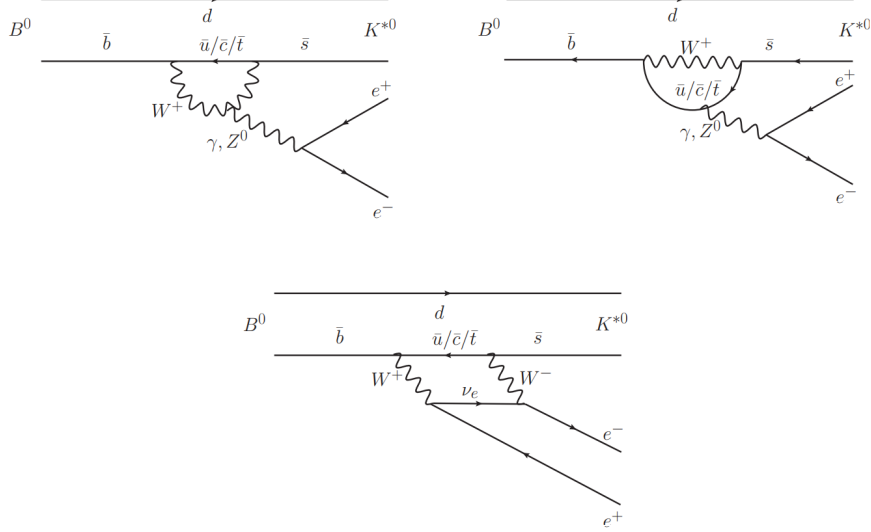


Figure 4: The three Feynman dominant diagrams contributing to the decay $B^0 \rightarrow K^{*0} e^+ e^-$ within the Standard Model [4].

By taking the ratio of the decays with electron and muon final states, we can construct observables that remain mostly insensitive to hadronic effects, which account for only around 1% effect in these observables [5]. Due to this limited hadronic effect, the Standard Model predictions for these values are very accurate. When comparing muons and electrons, these predictions are very close to unity due to the fact that the muon mass and electron mass difference is relatively small. The resulting ratios for these decays are better known as \mathcal{R}_K and \mathcal{R}_{K^*} :

$$\mathcal{R}_K = \frac{\mathcal{B}(B^+ \rightarrow K^+ \mu^- \mu^+)}{\mathcal{B}(B^+ \rightarrow K^+ e^- e^+)}, \quad (1)$$

$$\mathcal{R}_{K^*} = \frac{\mathcal{B}(B^+ \rightarrow K^{*+} \mu^- \mu^+)}{\mathcal{B}(B^+ \rightarrow K^{*+} e^- e^+)}. \quad (2)$$

A recent analysis performed by the LHCb collaboration has found a value of $\mathcal{R}_K = 0.745^{+0.090}_{-0.074} \pm 0.036$ which is 2.5σ deviations from the SM prediction [6]. The results for \mathcal{R}_K and \mathcal{R}_{K^*} by Belle and BABAR are summarized in figure 5 for different momentum ranges. The Belle and BABAR results seem to be in good agreement with the Standard Model prediction but suffer from a high level of uncertainty.

The $B^0 \rightarrow K^{*0} J/\psi(\rightarrow e^+ e^-)$ decay that is analysed in this thesis is used as a normalisation channel for the \mathcal{R}_{K^*} analysis done by LHCb (see Ref. [6]). Because of a tree level diagram contributing to the $B^0 \rightarrow K^{*0} J/\psi(\rightarrow e^+ e^-)$ decay the branching fraction of this decay is much higher than the $B^0 \rightarrow K^{*0} e^+ e^-$ decay which only happens at loop and box level. The tree level diagram makes that there are many more events to work with the on-shell J/ψ decay compared to the rare decay. Lepton universality is tested to hold to a high level in $B^0 \rightarrow K^{*0} J/\psi(\rightarrow \ell^- \ell^+)$ [3].

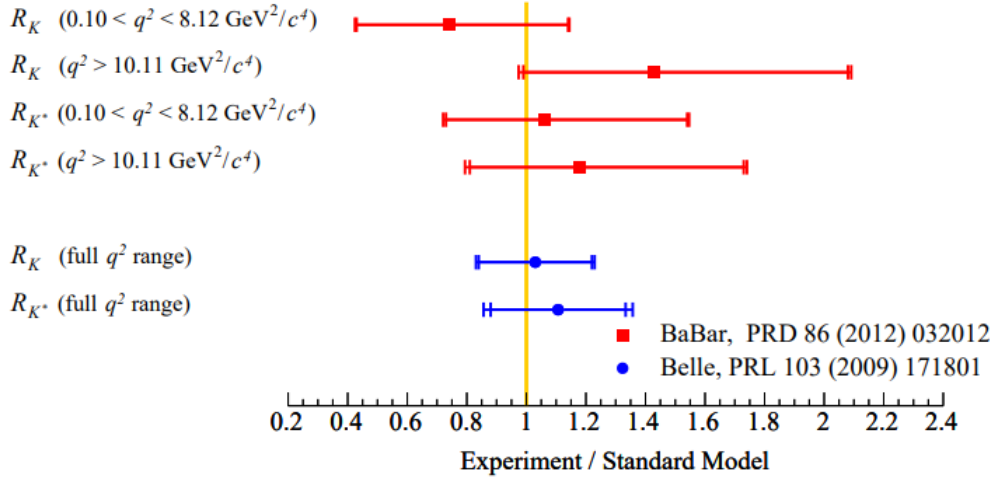


Figure 5: Summary of \mathcal{R}_K and \mathcal{R}_{K^*} results of the Belle and BABAR experiments [5]. The yellow line indicates the SM prediction of 1.

1.3.1 Angular analysis of the decay $B^0 \rightarrow K^{*0} \ell \bar{\ell}$

In order to get a better grasp on the \mathcal{R}_K and \mathcal{R}_{K^*} results, one can do an angular analysis of the involved decays. For the angular analysis of these decays one can analyse the distribution of angles that the final state particles propagate in. The SM also predict the angular behaviour of these types of decays. These predictions can be tested experimentally. In this thesis, we will present an angular analysis of the decay $B^0 \rightarrow K^{*0} J/\psi (\rightarrow e^+ e^-)$ that is closely related to the decay $B^0 \rightarrow K^{*0} e^+ e^-$. The decay via a prompt J/ψ , is much less rare than the $B^0 \rightarrow K^{*0} e^+ e^-$ decay, but results in the same final state. The angular analysis of this decay serves as a good test of how well the detector is understood, and is therefore an important first step in the angular analysis of the rare decay $B^0 \rightarrow K^{*0} e^+ e^-$. It is also used as a normalisation channel in the analysis of the rare decay.

The angular analysis of the decay $B^0 \rightarrow K^{*0} \mu^- \mu^+$ has been studied by LHCb extensively [7, 8, 9]. The angular analysis of the decay with final state electrons has also been performed for electrons in the low q^2 region [4]. In this low q^2 region, the decay is dominated by the coupling of the lepton pair to a virtual photon, $B^0 \rightarrow K^{*0} \gamma \rightarrow (e^- e^+)$. Experimentally, decays with final state muons are easier to analyse than with final state electrons in LHCb. This is because electrons undergo bremsstrahlung due to their interaction with the Coulomb field of the atoms that make up the detector. This interaction scales with E/m_l^2 , where m_l is the lepton mass. Because the mass of the electron is smaller than the mass of the muon the electrons are more affected by bremsstrahlung.

When electrons undergo bremsstrahlung they emit a photon. This photon can be detected by LHCb's Electromagnetic Calorimeter, ECAL (see 2.3.2), and the photon energy can be added back to the electron energy when the electron is reconstructed. A shortcoming here is that the ECAL energy resolution is limited, and not all photons are detected by the ECAL. However, the decays with final state electrons are of great interest because they constitute part of the \mathcal{R}_K and \mathcal{R}_{K^*} observables. Therefore considerable effort is put towards the improvement of the analysis by the LHCb collaboration.

2 Detector

The data used in this analysis was collected by the LHCb detector [10] at CERN. This detector is located at the Large Hadron Collider (LHC) particle accelerator. The LHC is the world's largest particle accelerator, and can operate at the highest beam pipe energy. The LHC accelerates particles in a two ring synchrotron that is being fed by multiple pre-accelerators. The LHC ring itself is 27km in circumference. Protons can be collided at a center of mass energy of 13 TeV. Along the circumference there are four interaction points. At each of these interaction points there are particle detectors with different properties to enable the probing of different aspects of particle physics. The four main detectors are:

- The LHCb (Large Hadron Collider beauty [10]) detector is a forward spectrometer. This detector primarily measures CP violation with b and c quarks. The goal of this experiment is to study the difference between matter and anti-matter. The physics program has expanded over time, and now also covers e.g. exotica, strange physics and heavy ions.
- ATLAS (A Toroidal LHC ApparatuS [11]) and CMS (Compact Muon Solenoid [12]) are general-purpose detectors. One of the fields of study at these detectors are the properties of the Higgs boson.
- ALICE (A Large Ion Collider Experiment [13]) is a detector optimized for heavy-ion collisions. These collisions produce a state of matter which is called the quark-gluon plasma, which is being analysed by the ALICE collaboration.

Also rare decays of beauty and charm hadrons are being analysed at LHCb. Because of these specific physics goals the LHCb detector has characteristics that differ from more general purpose detectors like ATLAS and CMS. The most obvious one is the geometry of the detector. The detector is a single-arm forward detector. This is due to the fact that at high energies B hadrons are produced primarily in the forward and backward cone [10].

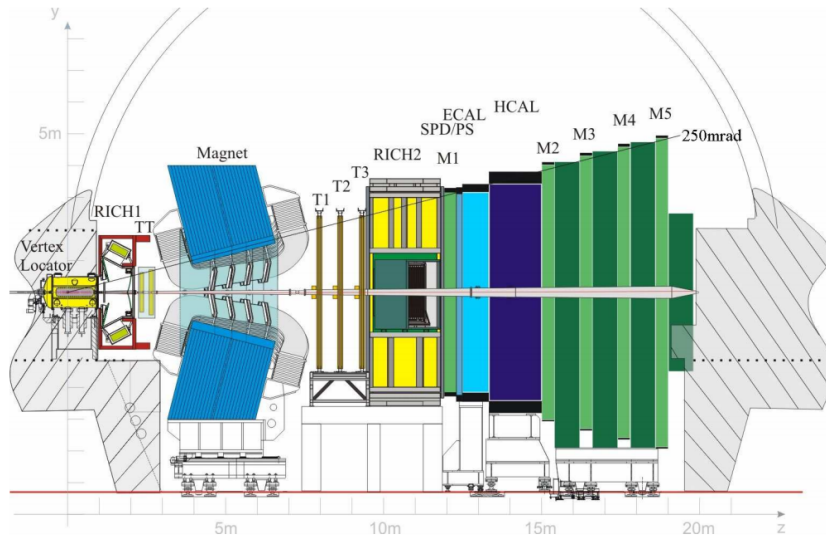


Figure 6: Schematic side view of the LHCb detector [10].

2.1 Magnet

LHCb is fitted with a dipole magnet for bending charged particles. The purpose of this bending is to determine the particle momentum from the curvature of each track. The magnet is made of two coils that weigh 54 tons. They are surrounded by an iron yoke of 1500 tons. It is designed to have the highest strength possible in the region between the VELO (2.2.1) and the TT station (2.2.2) while having a field strength of less than 2 mT inside of the RICH detectors. The total field integral of the magnet is 4 Tm for a track with a length of 10 meters. Figure 7 shows the strength of the magnet. The polarity of the magnet is changed periodically to reduce systematic effects, which is especially relevant for CP studies.

To have a good understanding of the magnetic field inside the detector several magnetic field measurement campaigns have been done. This is important for having a good momentum resolution for charged particles. The magnetic field needs to be known with a precision of 10^{-4} , with the peak of the field known to within a few millimeters. The magnetic field is mapped with a 4×10^{-4} precision inside of the detector.

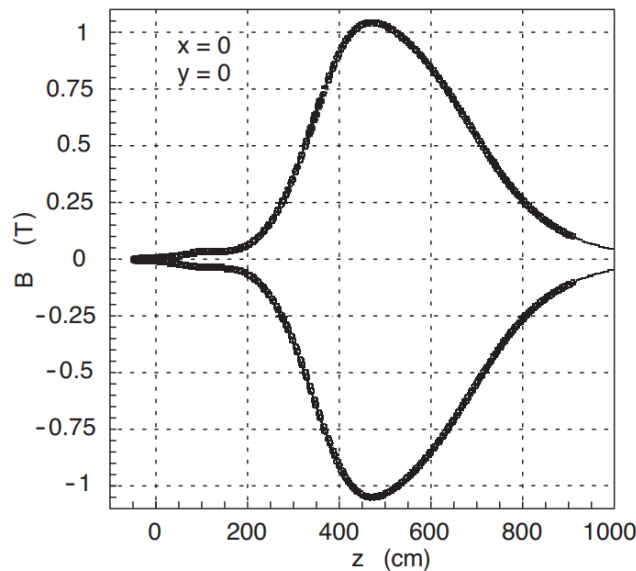


Figure 7: Strength of the magnetic field along the beam pipe of the LHCb detector [10].

2.2 Tracking

The LHCb consists of various subdetectors that are used in the tracking of particles. The first detector is the Vertex Locator which is very close to the beam pipe and important for reconstructing secondary vertices. The next detector is the Silicon Tracker (ST) which consists of the Tracker Turicensis (TT) and the Inner Tracker (IT) detectors. The last detector for tracking is the Outer Tracker (OT) which is equipped for tracking charged particles and measuring their momentum.

2.2.1 VERtEX LOcator (VELO)

The detector closest to the beam pipe is the VERtEX LOcator, or VELO. This detector provides very precise measurements of the particle tracks close to the interaction points. A distinctive feature of b and c -hadron decays is the displaced secondary vertex. The VELO plays a crucial role in identifying these secondary vertices. It consists of a series of silicon modules. Each of the modules provides measurements on the cylindrical r and ϕ coordinates along the beam pipe. The modules are placed closer to the beam than allowed for by the LHC during injection. To overcome this problem the VELO modules can be retracted. Figure 8 shows the front face of the modules in fully closed and retracted positions. Also shown is the placement of the VELO modules along the beam pipe.

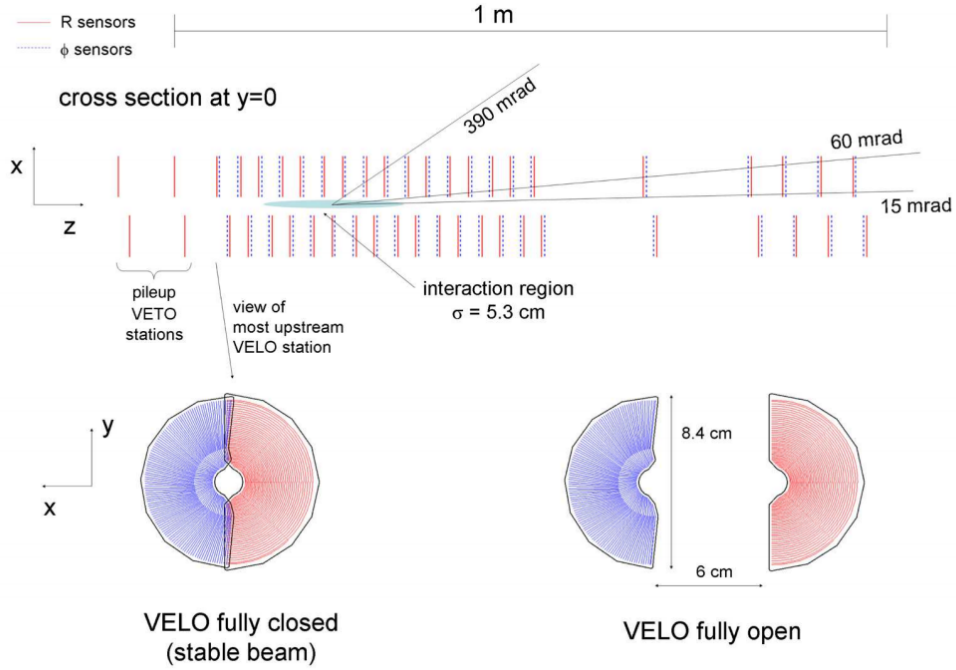


Figure 8: Cross section of the VELO silicon sensors. Also illustrated is the front face of the first modules in both closed and open positions [10].

The requirements for the VELO detector are very high as the ability of reconstructing vertices with a high precision is one of the most important features of the LHCb detector. Without this precise reconstruction it would not be possible to have precise measurements of decay lifetimes and impact parameters. It also plays an important role in determining the flavour of the particles that are produced.

2.2.2 Tracker Turicensis (TT)

The Tracker Turicensis (TT) uses microstrip sensors made of silicon. It serves as an extension of the VELO. The TT detector station is placed upstream of the magnet and is a 150 cm wide and 130 cm high planar tracking station. The active area of the TT is about 8.4 m². It is made up of four detection layers that are arranged in a $(x-u-v-x)$ pattern. Here the inner and outer x , layers are vertical strips with the middle, u and v , layers rotated at a stereo angle of -5° and $+5^\circ$ respectively. The TT is shown in purple in figure 9 upstream from the magnet (negative z direction).

2.2.3 Inner Tracker (IT)

The Inner Tracker is positioned downstream of the magnet and consists of three stations, the T1, T2 and T3. They are also made up of four detection layers that are arranged in the same $(x-u-v-x)$ pattern as the TT. The purpose of this geometry is to facilitate the 3D reconstruction of tracks. The detectors have a strip pitch of around $200\ \mu\text{m}$ and achieve a hit resolution of $50\ \mu\text{m}$. The IT covers an active area of $4.0\ \text{m}^2$. Figure 9 shows the IT in purple, placed downstream (positive z direction) from the magnet.

2.2.4 Outer Tracker (OT)

The Outer Tracker (OT) is a drift-time detector that is used for the tracking of charged particles and the measurement of their momentum. It covers a large acceptance area. The OT is made from gas-tight straw-tube modules that are arranged in an array. Modules are built containing two staggered monolayers or drift tubes. Their inner diameter is $4.9\ \text{mm}$. The modules are arranged in three distinct stations that are shown in blue figure 9.

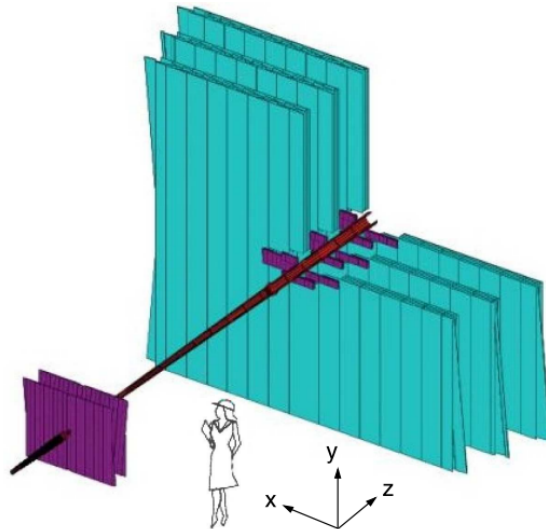


Figure 9: Arrangement of the TT, IT and TT detectors. The TT and IT are shown in purple on the negative and positive z direction respectively. The OT is shown in blue. The z direction is along the beam pipe [10].

The tubes are filled with a mixture of 70% Argon and 30% CO_2 . This mixture is chosen because it provides a fast drift time of below $50\ \text{ns}$ while having a sufficient drift-coordinate resolution of around $200\ \mu\text{m}$. The three OT stations each consist of four layers that are arranged in a $(x-u-v-x)$ geometry. Like the Silicon Tracker the u and v layers are tilted with $\pm 5^\circ$ with respect to the x layers respectively.

To facilitate the precise measurement of the invariant mass of reconstructed B mesons an excellent momentum resolution is required. To achieve this, information from the IT and OT is combined. For example, in order to have a mass resolution of $10\ \text{MeV}/c^2$ in the decay $B_s^0 \rightarrow D_s^- \pi^+$, one would need a momentum resolution of $\delta p/p \approx 0.4\%$. For B meson decays with a high multiplicity, we also need a high tracking efficiency, while having as

little as possible wrongly reconstructed tracks. To achieve a 80% reconstruction efficiency for the decay $B_s^0 \rightarrow D_s^- \pi^+$, a track efficiency of 95% would be needed [10].

2.3 Particle identification

Particle identification (PID) is of crucial importance to the LHCb experiment. The capacity to distinguish between pions and kaons is especially important in the analysis of B hadron decays. For this, the LHCb detector uses three subdetectors. They are the Ring Imaging Cherenkov detectors, or RICH, the calorimeters and the muon system [14].

2.3.1 RICH

For large polar angles momentum spectra get softer and at small polar angles the momentum spectra get harder. For this reason LHCb is equipped with two RICH detectors. The two detectors cover a different momentum range and are complementary to each other. The RICH1 detector is suitable for detecting low momentum charged particles in the range of 1 to 60 GeV. RICH1 is placed upstream of the magnet. It uses both C_4F_{10} and aerogel radiators. The RICH2 detector is suitable for detecting higher momentum particles and covers a momentum range from ~ 15 GeV to beyond ~ 100 GeV. The RICH2 detector is placed downstream from the magnet and it uses a CF_4 radiator. The Cherenkov angle for particles inside of the different materials as function of the particle momentum is given in figure 10.

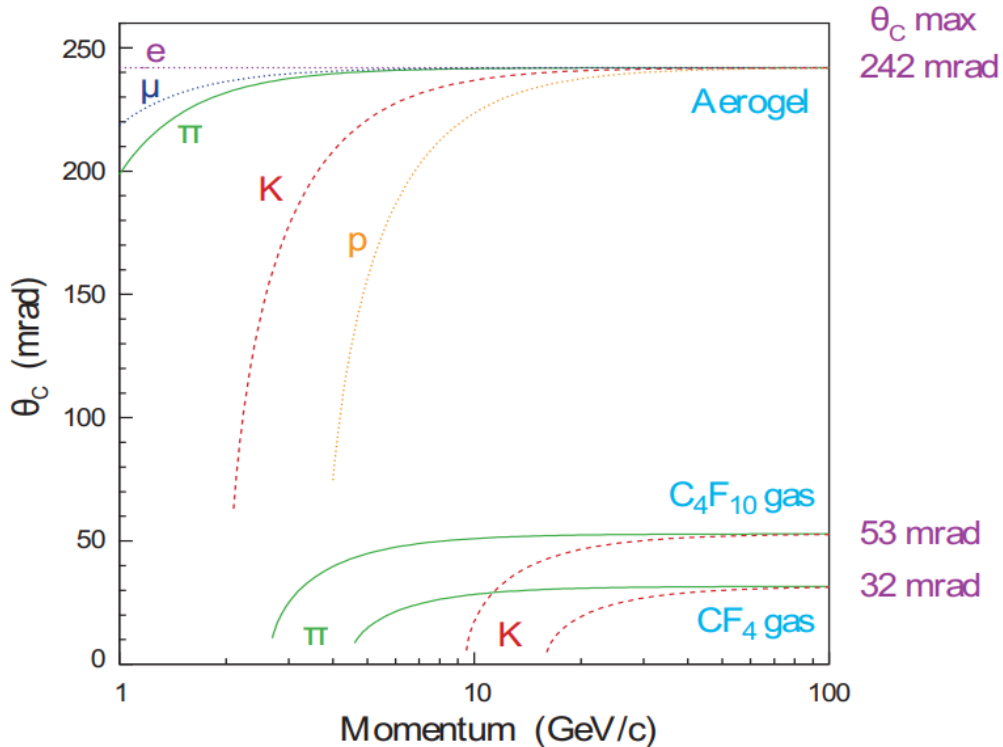


Figure 10: Cherenkov angle for different RICH radiator materials versus particle momentum. Using different radiator materials facilitates a large momentum coverage [10].

2.3.2 Calorimeter

The calorimeter in LHCb is used for several different functions. One such is the identification of electrons, photons and hadrons. Their energy and position is also determined using the calorimeter system. To be able to successfully determine the flavour of particles, which is crucial for LHCb, the reconstruction of π^0 and prompt photons is of great importance. Prompt photons are the photons that are created in the collision, and thus do not originate from material interactions.

The calorimeter system used by LHCb consists of two parts. The first part of the calorimeter is the electromagnetic calorimeter (ECAL). The ECAL is followed by a hadron calorimeter (HCAL). The basic principle of a calorimeter is the detection of scintillation light by a Photo-Multiplier (PMT). This is used in the ECAL and HCAL calorimeters. The gain of the PMTs scales with their distance to the beam pipe to have a constant transverse energy scale. Over the surface of the calorimeters, the hit density varies by two orders of magnitude. To account for this the ECAL is made of three sections and the HCAL of two sections each with different cell sizes. The layout of these sections is shown in figure 11.

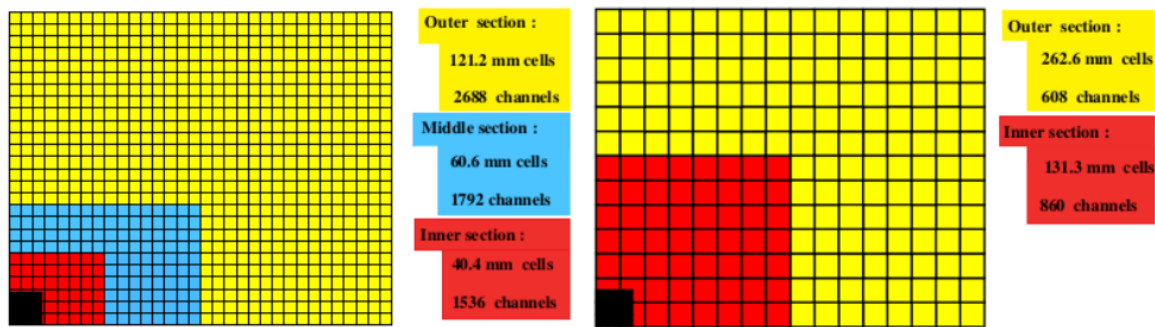


Figure 11: Arrangement of the ECAL (left) and HCAL (right) segmentation. The upper right quarter of both detector front faces is shown [10]. The black square represent the position of the beam pipe.

2.3.3 Muon system

The third type of detector used for PID is the muon system, that is specifically designed for muon identification. Because decays with muons are very relevant for most LHCb analysis, this detector is of great importance. Many CP sensitive B meson decays have final state muons, such as the flagship decay for the CP asymmetry and oscillation measurements $B_s^0 \rightarrow J\psi(\rightarrow \mu^+\mu^-)\phi$.

The system is made up of five rectangular stations, called M1 thru M5. The five stations constitute a total of 1380 chambers that cover an area of 435m^2 . Systems M2-M5 are placed behind the calorimeters, while system M1 placed in front of the calorimeters as shown in figure 12 (a). All five stations are divided into four regions with their dimensions scaling with their distance from the beam pipe such that all regions have roughly the same occupancy. Figure 12 (b) shows a front face view of the four regions.

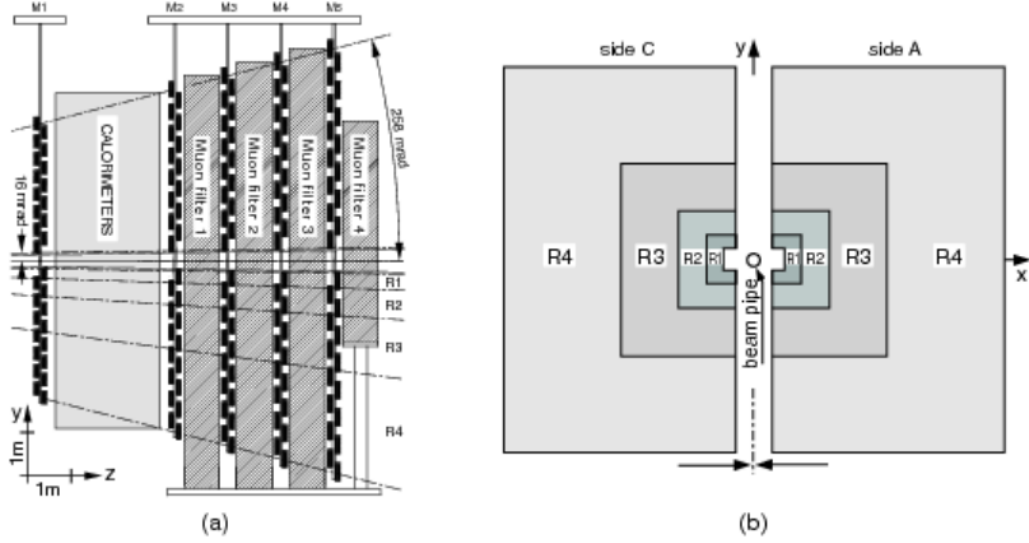


Figure 12: (a) Side view of the muon system. The muon systems M2-M5 are placed after the calorimeters. system M1 is placed before the calorimeters. (b) Front view of the four detector regions [10].

2.3.4 Final PID

The information of the different detectors is combined for the final PID:

- The calorimeters play a big role in distinguishing photons, electrons and neutral pions. Electrons leave a energetic deposition on the calorimeter while neutral particles such as the photon and π^0 do not. For the classification in the calorimeter a neural network classifier is used.
- The RICH plays a big role in differentiating between charged hadrons. RICH also contributes complementary information on charged leptons.
- The identification of muons happens in the muon system.

The final PID is computed as the sum of the different likelihoods. Other multivariate computing techniques can be deployed to compute a single PID value for each candidate particle hypothesis.

2.4 Trigger

The trigger in LHCb serves an important role. It reduces the crossing frequency of interactions that are stored for offline analysis from 40MHz to 12.5kHz. The LHCb trigger consists of two levels, the Level-0, or L0, and the High Level Trigger (HLT). The main objective of the L0 trigger is to obtain a high efficiency in selecting events for offline analysis while storing as little background events as possible. The L0 trigger does this by using information from the calorimeters and muon chambers. It is built around custom electronics to handle the high bunch crossing frequency of 40 MHz. With this, it reduces the beam crossing rate of 40 MHz to 1 MHz, at which point the detector can be read out. The information from the three detection elements is collected in the L0 Decision Unit where the trigger decision is made.

The High Level Trigger (HLT) uses the full event data to select events. HLT1 reduces the output rate of events to 100 kHz, after which HLT2 further reduces it to 12.5 kHz. At this rate the events selected by the HLT are stored permanently. HLT consists of a C++ application that is run on over 2000 computing nodes. The HLT is divided into two parts, HLT1 and HLT2. In HLT1 the candidates from L0 are confirmed and have further information added from detectors such as the VELO. The HLT2 stage then selects tracks with broad cuts on momenta and impact parameters. These are then used to form composite particles on which further selection is applied. Selection cuts at trigger level are generally relaxed to facilitate the study of selection sensitivity and to potentially benefit from refined calibration constants. A schematic view of the LHCb trigger is shown in figure 13.

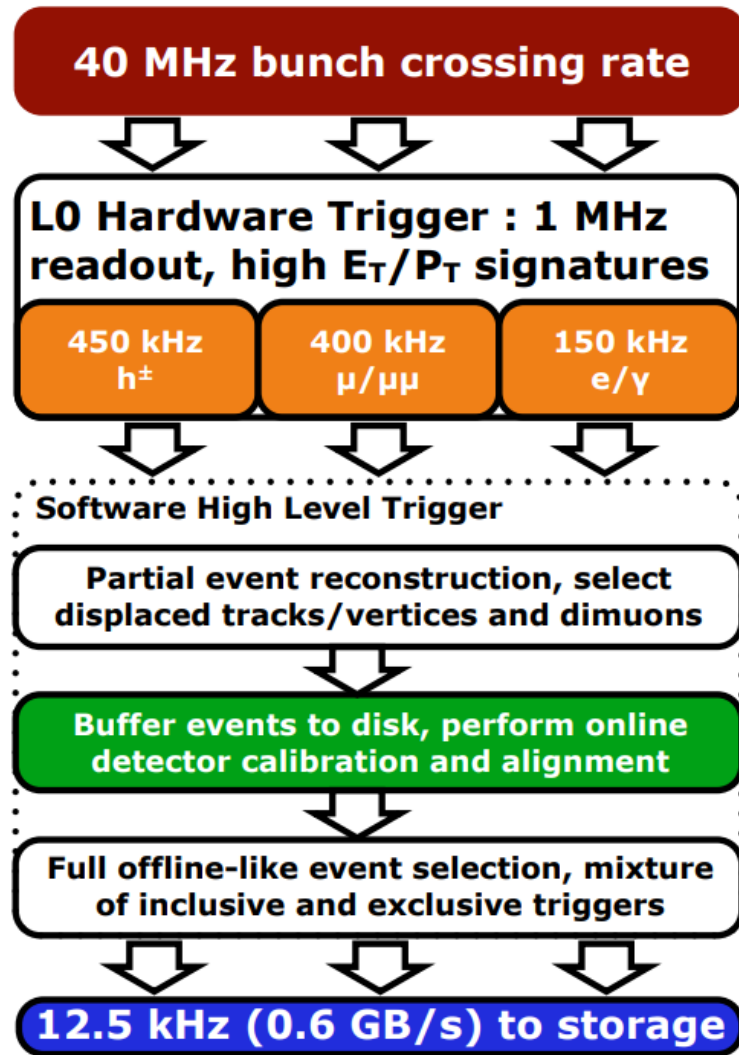


Figure 13: A schematic view of the LHCb trigger showing the two trigger components: L0 and HLT. This figure was taken from an internal LHCb presentation on the trigger system.

3 Analysis Strategy

3.1 Definition of decay angles

For the angular analysis of the $B^0 \rightarrow K^{*0} J/\psi (\rightarrow e^+ e^-)$ decay it is important to have a clear definition of the decay angles. The conventions used for this differ between theorists and experimentalists. In this thesis we will use the convention used by the LHCb collaboration [9]. The definition that is conventionally used by theorists is defined in [15].

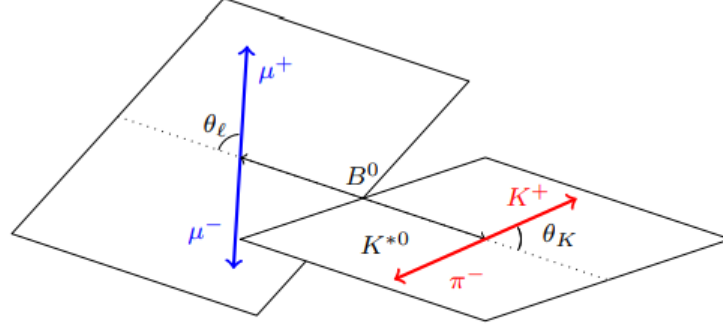
The final state of the decay, $K^{*0} (\rightarrow K\pi) \ell^+ \ell^-$, can be described by three decay angles, $\vec{\Omega} = (\cos \theta_l, \cos \theta_K, \phi)$, and the invariant mass of the dilepton system squared, q^2 . In this convention the θ_l is defined as the angle between the direction of the $\ell^+ (\ell^-)$ and the opposite of the direction of the $B^0 (\bar{B}^0)$ in the dilepton rest frame. The θ_K angle is given by the angle of the kaon direction with the opposite of the direction of the $B^0 (\bar{B}^0)$ in the $K^{*0} (\bar{K}^{*0})$ rest frame. Lastly the ϕ angle is given by the angle between the $\ell^+ \ell^-$ plane and the plane given by the kaon and pion which originate from the K^{*0} in the $B^0 (\bar{B}^0)$ rest frame.

A graphical representation of the definition of the decay angles is shown in figure 14. The explicit expressions of the angles for B^0 are defined as

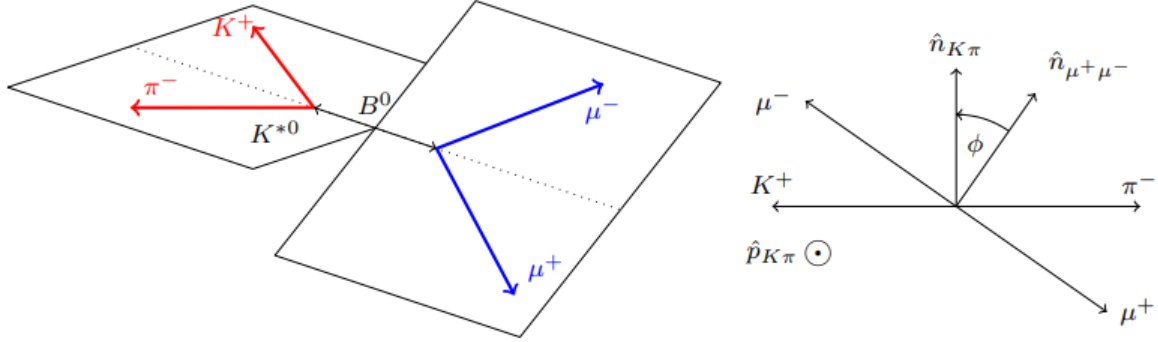
$$\begin{aligned} \cos \theta_l &= \left(\hat{p}_{\mu^+}^{(\mu^+ \mu^-)} \right) \cdot \left(\hat{p}_{\mu^+ \mu^-}^{(B^0)} \right) = \left(\hat{p}_{\mu^+}^{(\mu^+ \mu^-)} \right) \cdot \left(-\hat{p}_{B^0}^{(\mu^+ \mu^-)} \right), \\ \cos \theta_K &= \left(\hat{p}_{K^+}^{(K^{*0})} \right) \cdot \left(\hat{p}_{K^{*0}}^{(B^0)} \right) = \left(\hat{p}_{K^+}^{(K^{*0})} \right) \cdot \left(-\hat{p}_{B^0}^{(K^{*0})} \right), \\ \cos \phi &= \left(\hat{p}_{\mu^+}^{(B^0)} \times \hat{p}_{\mu^-}^{(B^0)} \right) \cdot \left(\hat{p}_{K^+}^{(B^0)} \times \hat{p}_{\pi^-}^{(B^0)} \right), \\ \sin \phi &= \left[\left(\hat{p}_{\mu^+}^{(B^0)} \times \hat{p}_{\mu^-}^{(B^0)} \right) \times \left(\hat{p}_{K^+}^{(B^0)} \times \hat{p}_{\pi^-}^{(B^0)} \right) \right] \cdot \hat{p}_{K^{*0}}^{(B^0)}. \end{aligned} \tag{3}$$

And for \bar{B}^0 they are defined as

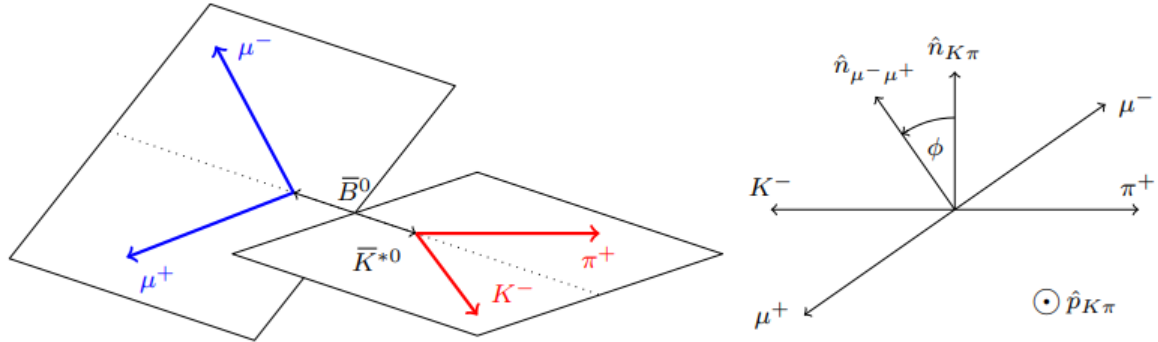
$$\begin{aligned} \cos \theta_l &= \left(\hat{p}_{\mu^-}^{(\mu^+ \mu^-)} \right) \cdot \left(\hat{p}_{\mu^+ \mu^-}^{(\bar{B}^0)} \right) = \left(\hat{p}_{\mu^-}^{(\mu^+ \mu^-)} \right) \cdot \left(-\hat{p}_{\bar{B}^0}^{(\mu^+ \mu^-)} \right), \\ \cos \theta_K &= \left(\hat{p}_{K^-}^{(K^{*0})} \right) \cdot \left(\hat{p}_{K^{*0}}^{(\bar{B}^0)} \right) = \left(\hat{p}_{K^-}^{(K^{*0})} \right) \cdot \left(-\hat{p}_{\bar{B}^0}^{(K^{*0})} \right), \\ \cos \phi &= \left(\hat{p}_{\mu^-}^{(\bar{B}^0)} \times \hat{p}_{\mu^+}^{(\bar{B}^0)} \right) \cdot \left(\hat{p}_{K^-}^{(\bar{B}^0)} \times \hat{p}_{\pi^+}^{(\bar{B}^0)} \right), \\ \sin \phi &= - \left[\left(\hat{p}_{\mu^-}^{(\bar{B}^0)} \times \hat{p}_{\mu^+}^{(\bar{B}^0)} \right) \times \left(\hat{p}_{K^-}^{(\bar{B}^0)} \times \hat{p}_{\pi^+}^{(\bar{B}^0)} \right) \right] \cdot \hat{p}_{\bar{K}^{*0}}^{(\bar{B}^0)}. \end{aligned} \tag{4}$$



(a) θ_K and θ_ℓ definitions for the B^0 decay



(b) ϕ definition for the B^0 decay



(c) ϕ definition for the \bar{B}^0 decay

Figure 14: A graphical representation of the definition of the decay angles θ_K , θ_l and ϕ as they are used by LHCb [9] and in this thesis.

3.2 Angular PDF

The decay rate of the $B^0 \rightarrow K^{*0} e^+ e^-$ decay is given by the sum [8]

$$\frac{d^4\Gamma[B^0 \rightarrow K^{*0} e^+ e^-]}{dq^2 d\vec{\Omega}} = \frac{9}{32\pi} \sum_i I_i(q^2) f_i(\vec{\Omega}), \quad (5)$$

and for its charge conjugate $\bar{B}^0 \rightarrow \bar{K}^{*0} e^- e^+$ by

$$\frac{d^4\Gamma[\bar{B}^0 \rightarrow \bar{K}^{*0} e^- e^+]}{dq^2 d\vec{\Omega}} = \frac{9}{32\pi} \sum_i \bar{I}_i(q^2) f_i(\vec{\Omega}). \quad (6)$$

In these expressions the f_i terms are combinations of spherical harmonics that depend on the value of $\vec{\Omega} = (\cos \theta_l, \cos \theta_K, \phi)$. The I_i terms are q^2 dependent angular observables that can be expressed as bilinear combinations of eight complex decay amplitudes, $A_{\perp}^{L,R}$, $A_{\parallel}^{L,R}$, $A_0^{L,R}$, A_t and A_{Scalar} . The decay amplitudes correspond to different transversity states of the K^{*0} meson and left- and right-handed chirality states of the dilepton system. The angular observables follow the relations [15]:

$$\begin{aligned} I_1^s &= \frac{(2 + \beta_e^2)}{4} [|A_{\perp}^L|^2 + |A_{\parallel}^L|^2 + |A_{\perp}^R|^2 + |A_{\parallel}^R|^2] + \frac{4m_e^2}{q^2} \text{Re}(A_{\perp}^L A_{\perp}^{R*} + A_{\parallel}^L A_{\parallel}^{R*}), \\ I_1^c &= |A_0^L|^2 + |A_0^R|^2 + \frac{4m_e^2}{q^2} [|A_t|^2 + 2 \text{Re}(A_0^L A_0^{R*})] + \beta_e^2 |A_{\text{Scalar}}|^2, \\ I_2^s &= \frac{\beta_e^2}{4} [|A_{\perp}^L|^2 + |A_{\parallel}^L|^2 + |A_{\perp}^R|^2 + |A_{\parallel}^R|^2], \\ I_2^c &= -\beta_e^2 [|A_0^L|^2 + |A_0^R|^2], \\ I_3 &= \frac{1}{2} \beta_e^2 [|A_{\perp}^L|^2 - |A_{\parallel}^L|^2 + |A_{\perp}^R|^2 - |A_{\parallel}^R|^2], \\ I_4 &= \frac{1}{\sqrt{2}} \beta_e^2 [\text{Re}(A_0^L A_{\parallel}^{L*}) + \text{Re}(A_0^R A_{\parallel}^{R*})], \\ I_5 &= \sqrt{2} \beta_e \left[\text{Re}(A_0^L A_{\perp}^{L*}) - \text{Re}(A_0^R A_{\perp}^{R*}) - \frac{m_e}{\sqrt{q^2}} \text{Re}(A_{\parallel}^L A_{\text{Scalar}}^* + A_{\perp}^R A_{\text{Scalar}}^*) \right], \\ I_6^s &= 2\beta_e [\text{Re}(A_{\parallel}^L A_{\parallel}^{L*}) - \text{Re}(A_{\parallel}^R A_{\parallel}^{R*})], \\ I_6^c &= 4\beta_e \frac{m_e}{\sqrt{q^2}} \text{Re}[A_0^L A_{\text{Scalar}}^* + A_0^R A_{\text{Scalar}}^*], \\ I_7 &= \sqrt{2} \beta_e \left[\text{Im}(A_0^L A_{\parallel}^{L*} - A_0^R A_{\parallel}^{R*}) + \frac{m_e}{\sqrt{q^2}} \text{Im}(A_{\perp}^L A_{\text{Scalar}}^* + A_{\perp}^R A_{\text{Scalar}}^*) \right], \\ I_8 &= \frac{1}{\sqrt{2}} \beta_e^2 [\text{Im}(A_0^L A_{\perp}^{L*}) + \text{Im}(A_0^R A_{\perp}^{R*})], \\ I_9 &= \beta_e^2 [\text{Im}(A_{\parallel}^{L*} A_{\perp}^L) + \text{Im}(A_{\parallel}^{R*} A_{\perp}^R)], \end{aligned} \quad (7)$$

with $\beta_e = \sqrt{1 - 4m_e^2/q^2}$ where m_e is the electron rest mass. The superscript, s or c , indicates the dependence on $\sin^2(\theta_k)$ or $\cos^2(\theta_k)$ respectively of the associated spherical harmonic. From these decay amplitudes twelve CP average coefficients,

$$S_i^{(s,c)} = (I_i^{(s,c)} + \bar{I}_i^{(s,c)}) \left/ \frac{d(\Gamma + \bar{\Gamma})}{dq^2} \right. \quad (8)$$

and twelve CP asymmetry coefficients,

$$A_i^{(s,c)} = (I_i^{(s,c)} - \bar{I}_i^{(s,c)}) \left/ \frac{d(\Gamma + \bar{\Gamma})}{dq^2} \right. \quad (9)$$

can be defined. The decay amplitude A_{Scalar} corresponds to the decay being mediated by a scalar operator and is affected by the lepton mass. In this analysis we consider it to be zero. It could however be a potential observable for a NP scalar current [15]. The decay amplitude A_t corresponds to a virtual gauge boson from a K^* in longitudinal polarization in its own rest frame, and a V^* in a time-like polarization in its own rest frame, where the V^* can represent either a photon or Z boson that couples to the J/ψ ,

$$A_t = \mathcal{M}_{(0,t)}(B \rightarrow K^* V^*). \quad (10)$$

For q^2 much larger than the electron rest mass, the electron rest mass of the final state electrons can be considered negligible. In this massless limit A_t also vanishes, as it scales with the electron rest mass. The CP averaged observables hold the following relations

$$S_1^s = 3S_1^c = -S_2^c, \quad (11)$$

$$\frac{3}{4}(2S_1^s + S_1^c) - \frac{1}{4}(2S_2^s + S_2^c) = 1. \quad (12)$$

This reduces the number of independent CP averaged observables (eq. 8) from twelve to eight. The observable S_1^c is related to the longitudinal polarisation of the K^{*0} meson and is often referred to as F_L . The observable S_6^s is related to the forward-backward asymmetry, $A_{FB} = \frac{3}{4}S_6^s$. Because we do not discriminate between charge conjugate decays in this analysis, all CP asymmetric terms drop out from our final PDF. The full angular distribution of the decay can then be written as

$$\begin{aligned} \frac{1}{d(\Gamma + \bar{\Gamma})/dq^2} \frac{d^4(\Gamma + \bar{\Gamma})}{dq^2 d\vec{\Omega}} &= \frac{9}{32\pi} \left[\frac{3}{4}(1 - F_L) \sin^2 \theta_K + F_L \cos^2 \theta_K \right. \\ &\quad + \frac{1}{4}(1 - F_L) \sin^2 \theta_K \cos 2\theta_l \\ &\quad - F_L \cos^2 \theta_K \cos 2\theta_l + S_3 \sin^2 \theta_K \sin^2 \theta_l \cos 2\phi \\ &\quad + S_4 \sin 2\theta_K \sin 2\theta_l \cos \phi + S_5 \sin 2\theta_K \sin \theta_l \cos \phi \\ &\quad + \frac{4}{3}A_{FB} \sin^2 \theta_K \cos \theta_l + S_7 \sin 2\theta_K \sin \theta_l \sin \phi \\ &\quad \left. + S_8 \sin 2\theta_K \sin 2\theta_l \sin \phi + S_9 \sin^2 \theta_K \sin^2 \theta_l \sin 2\phi \right]. \end{aligned} \quad (13)$$

This distribution corresponds to the resonant P-wave contribution of the K^{*0} system to the final state $K^+ \pi^- e^+ e^-$. The K^{*0} system can however also be in a S-wave configuration. In this configuration it has spin 0. In previous analysis the contribution of this S-wave was handled as a systematic uncertainty. We have included it in this analysis as part of the angular PDF. The S-wave introduces two additional complex amplitudes, $\mathcal{A}_S^{L,R}$. This results in six additional angular terms, and the angular distribution is modified to

$$\begin{aligned} \frac{1}{d(\Gamma + \bar{\Gamma})/dq^2} \frac{d^4(\Gamma + \bar{\Gamma})}{dq^2 d\vec{\Omega}} \Big|_{S+P} &= (1 - F_S) \frac{1}{d(\Gamma + \bar{\Gamma})/dq^2} \frac{d^4(\Gamma + \bar{\Gamma})}{dq^2 d\vec{\Omega}} \Big|_P \\ &+ \frac{3}{16\pi} F_S \sin^2 \theta_l \\ &+ \frac{9}{32\pi} (S_{11} + S_{13} \cos 2\theta_l) \cos \theta_K \\ &+ \frac{9}{32\pi} (S_{14} \sin 2\theta_l + S_{15} \sin \theta_l) \sin \theta_K \cos \phi \\ &+ \frac{9}{32\pi} (S_{16} \sin \theta_l + S_{17} \sin 2\theta_l) \sin \theta_K \sin \phi. \end{aligned} \quad (14)$$

Here F_S denotes the fraction of the S-wave,

$$F_S = \frac{|\mathcal{A}_S^L|^2 + |\mathcal{A}_S^R|^2}{|\mathcal{A}_S^L|^2 + |\mathcal{A}_S^R|^2 + |\mathcal{A}_0^L|^2 + |\mathcal{A}_0^R|^2 + |\mathcal{A}_\parallel^L|^2 + |\mathcal{A}_\parallel^R|^2 + |\mathcal{A}_\perp^L|^2 + |\mathcal{A}_\perp^R|^2}, \quad (15)$$

with $F_S = 3S_{10} = -S_{12}$. The terms S_{11} and S_{13} - S_{17} stem from the interaction of the S- and P-wave amplitude components.

3.3 Acceptance

Due to the geometry and inefficiencies of the LHCb detector, the observed angular distributions will differ from the true angular distributions. Such modification can also originate from effects in the trigger line, or by the cuts applied when selecting signal candidates. To compare final distributions to theory, it is important to model these acceptance effects correctly. The three dimensional detector acceptance is parameterised as

$$\epsilon(\cos \theta_l, \cos \theta_K, \phi) = \sum_{ijm} c_{ijm} L_i(\cos \theta_l) L_j(\cos \theta_K) L_m(\phi), \quad (16)$$

where c_{ijm} are coefficients, and the terms $L_a(x)$ denote Legendre polynomials of order a [16]. We can construct polynomials, $P_a(x)$, as

$$P_a(x) = L_a(x) \frac{2a+1}{2}, \quad (17)$$

that obey the orthonormality relation

$$\int_{-1}^{+1} P_a(x) P_b(x) dx = \delta_{ab}, \quad (18)$$

where δ_{ab} is the Kronecker delta [17]. In computing the coefficients of our parametrisation we use this orthonormality relation. Therefore we should only consider them on the range

of -1 to +1. We scale the ϕ argument to that range by dividing it by the value by π to get the argument to feed to the Legendre polynomial. To obtain the values of the coefficients c_{ijm} , we make use of a reconstructed Monte Carlo sample. For this Monte Carlo sample we know the values of the PDF parameters that were used to generate the events a priori. Therefore, we can compare the final reconstructed events that passed the detector acceptance to the input PDF to model the acceptance behaviour. The coefficients c_{ijm} are computed as

$$c_{ijm} = \frac{1}{N_{gen}} \sum_n^{N_{accepted}} \frac{P_i(\cos(\theta_l)_n) P_j(\cos(\theta_K)_n) P_m(\phi_n)}{PDF(\cos(\theta_l), \cos(\theta_K), \phi)}, \quad (19)$$

where $PDF(\cos(\theta_l)_n, \cos(\theta_K)_n, \phi_n)$ is the, a priori known, probability to generate an event with angles $\cos(\theta_l)$, $\cos(\theta_K)$ and ϕ during the production of the Monte Carlo sample. The sum over n indicates that we sum over all the events that are in the reconstructed Monte Carlo sample. In this analysis polynomials of up to order 6 are used. The acceptance parametrisation is shown in section 3.3.2 as a projection in the three angles $\cos(\theta_l)_n$, $\cos(\theta_K)_n$ and ϕ_n .

3.3.1 Normalisation

The final distribution that will be measured in the detector will be the product of the PDF describing the decay and the acceptance. In order to normalise the distribution of this product, its integral needs to be computed. The normalisation, \mathcal{N} , is calculated as:

$$\mathcal{N} = \int_1^1 d\cos\theta_l \int_1^1 d\cos\theta_K \int_{-\pi}^{\pi} d\phi \epsilon(\cos\theta_l, \cos\theta_K, \phi) \frac{1}{d(\Gamma + \bar{\Gamma})/dq^2} \frac{d^4(\Gamma + \bar{\Gamma})}{dq^2 d\vec{\Omega}} \Big|_{S+P}, \quad (20)$$

where $\epsilon(\cos\theta_l, \cos\theta_K, \phi)$ is the acceptance parametrisation. Because the acceptance parametrisation, (eq. 16), is constructed as a sum over coefficients, we can compute the integrals on a per coefficients basis and sum them,

$$\mathcal{N}(\cos\theta_l, \cos\theta_K, \phi) = \sum_{ijm} \int d\vec{\Omega} \epsilon_{ijm} \frac{1}{d(\Gamma + \bar{\Gamma})/dq^2} \frac{d^4(\Gamma + \bar{\Gamma})}{dq^2 d\vec{\Omega}} \Big|_{S+P}. \quad (21)$$

This computation is done using **SymPy**, a Python open-source library for analytical analysis [18]. Because the PDF depends only on geometric functions with the angles as arguments the computation is relatively straightforward. The analytical expression that we computed in this way is then implemented into the fitter.

3.3.2 Acceptance projections

In Figure 15 we show the projections of the acceptance parametrisation that was used in this analysis in the three angles $\cos\theta_K$, $\cos\theta_l$ and ϕ . For this parametrisation, coefficients of up to order 6 were calculated for all angles, using a reconstructed Monte Carlo sample containing $\sim 627k$ events. The blue dots represent the projection of the PDF angular distribution that was used in generating the sample, with the orange histogram showing the angular distribution of events that passed the detector acceptance. Both the PDF and the angular distribution of the sample were normalised to the same integral and rescaled to fit into the plot range. The yellow points represent the projection of the detector acceptance

and is calculated as the ratio of the reconstructed angular distribution with respect to the PDF angular distribution. The black points represent the projection of the acceptance parametrisation as it was used in this analysis. In the $\cos \theta_K$ angle the projections for the acceptance and acceptance parametrisation show a good agreement with each other. The parametrisation projection in the angle $\cos \theta_l$ shows similar behaviour, and overlaps the detector efficiency. For both angles the parametrisation seems to be too flat when compared to the acceptance. However, the deviation is very small in both angles. The acceptance parametrisation projection in the ϕ angle also shows a good agreement with the detector acceptance. For this angle the parametrisation seems to be too aggressive, with the minima being low and the maxima being high when compared to the detector acceptance. This deviation is also very small however.

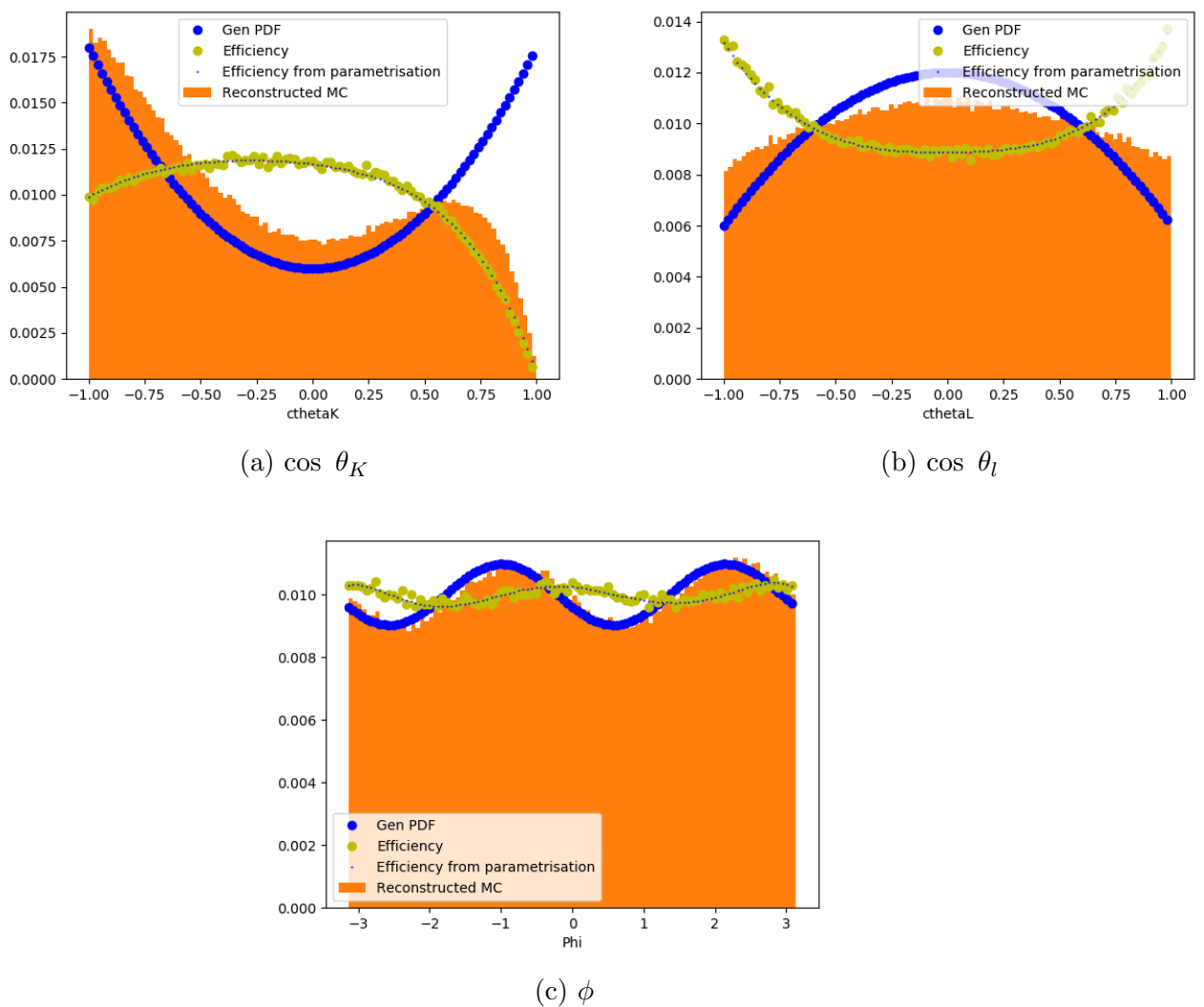


Figure 15: Angular distributions for the reconstructed Monte Carlo sample and the PDF it was generated with, together with the detector acceptance calculated from those distributions. The black points are calculated from the acceptance parametrisation that was used. The acceptance projection shows in general a good agreement with the detector acceptance, with only small deviations discernible.

4 Data and Selection

The data sample that is used in this analysis is the data obtained during the year 2016. This data set corresponds to a total integrated luminosity of 1.665 fb^{-1} at a total centre-of-momentum energy of 13 TeV. The selection process of the data sample can be divided into four steps:

1. Stripping line requirements
2. Trigger line requirements
3. Preselection with various event variable cuts
4. *sWeights* data weighting

After the selection, the total number of events left in the data sample is 31165.

4.1 Stripping

In LHCb, the BRUNEL [19] framework is used for reconstructing events in proton-proton collisions. For the data sample the reconstruction version **Reco16** was used. The data set was selected using stripping line **Stripping29r2p1** of stripping version **Bu2LLK_eeLine2** [20].

4.2 Trigger

The trigger lines that were used to generate this data sample are given in table 1 for all three levels. For an event to pass the trigger, it needs to pass at least one trigger line at every level.

Level	Trigger line	
L0	L0MuonDecision L0HadronDecision L0PhotonDecision	L0DiMuonDecision L0ElectronDecision
HLT1	Hlt1TrackMVADecision Hlt1TrackMVALooseDecision Hlt1TrackMuonDecision Hlt1DiMuonHighMassDecision Hlt1SingleMuonHighPTDecision Hlt1L0AnyDecision Hlt1SingleElectronNoIPDecision Hlt1GlobalDecision	Hlt1TwoTrackMVADecision Hlt1TwoTrackMVALooseDecision Hlt1TrackMuonMVADecision Hlt1DiMuonLowMassDecision Hlt1DiMuonNoL0Decision Hlt1L0AnyNoSPDDecision Hlt1SingleMuonNoIPDecision
HLT2	Hlt2DiMuonBDecision Hlt2DiMuonDetachedHeavyDecision Hlt2DiMuonDetachedPsi2SDecision Hlt2DiMuonJPsiHighPTDecision Hlt2DiMuonPsi2SHighPTDecision Hlt2DiMuonZDecision Hlt2LowMultDiMuon_PSDecision Hlt2SingleMuonDecision Hlt2SingleMuonLowPTDecision Hlt2TopoMu2BodyBBDTDecision Hlt2TopoMu4BodyBBDTDecision Hlt2Topo3BodyBBDTDecision Hlt2Topo2BodySimpleDecision Hlt2Topo4BodySimpleDecision Hlt2TopoE3BodyBBDTDecision Hlt2TopoE2BodySimpleDecision Hlt2TopoE4BodySimpleDecision Hlt2Topo3BodyDecision Hlt2TopoE2BodyDecision Hlt2TopoE4BodyDecision Hlt2TopoEE3BodyDecision Hlt2TopoMu2BodyDecision Hlt2TopoMu4BodyDecision Hlt2TopoMuE3BodyDecision Hlt2TopoMuMu2BodyDecision Hlt2TopoMuMuDDDecision Hlt2TopoE.*Decision Hlt2Charm.*Decision	Hlt2DiMuonDetachedDecision Hlt2DiMuonDetachedJPsiDecision Hlt2DiMuonJPsiDecision Hlt2DiMuonPsi2SDecision Hlt2DiMuonSoftDecision Hlt2LowMultDiMuonDecision Hlt2LowMultMuonDecision Hlt2SingleMuonHighPTDecision Hlt2SingleMuonRareDecision Hlt2TopoMu3BodyBBDTDecision Hlt2Topo2BodyBBDTDecision Hlt2Topo4BodyBBDTDecision Hlt2Topo3BodySimpleDecision Hlt2TopoE2BodyBBDTDecision Hlt2TopoE4BodyBBDTDecision Hlt2TopoE3BodySimpleDecision Hlt2Topo2BodyDecision Hlt2Topo4BodyDecision Hlt2TopoE3BodyDecision Hlt2TopoEE2BodyDecision Hlt2TopoEE4BodyDecision Hlt2TopoMu3BodyDecision Hlt2TopoMuE2BodyDecision Hlt2TopoMuE4BodyDecision Hlt2TopoMuMu2BodyDecision Hlt2DiMuonDY.*Decision Hlt2Topo.*Decision Hlt2DiElectron.*Decision

Table 1: List of trigger requirements. An event needs to pass at least 1 trigger line at all three levels to be included in the sample.

4.3 Preselection

In order to further remove background events, cuts are applied to the events that passed the stripping and trigger. They consist of various PID and kinematic variable requirements. For the latter, `DecayTreeFitter` (DTF) [21] variables are used. The preselection cuts that are applied to the data sample are combined into different categories. The different categories and their efficiency are shown in table 2.

Preselection	MagDown	MagUp
B mass	50.91 %	50.91 %
TriggerPresel	55.68 %	55.78 %
MeerkatPresel ee	48.53 %	48.45 %
VetoPresel	86.01 %	86.08 %
VetoPresel Bplus	95.16 %	95.10 %
PIDPresel ee	79.11 %	79.23 %
GenericPresel	79.34 %	79.36 %
TighterKst0Presel	91.69 %	91.60 %
BDT	89.52 %	89.31 %
q^2 Cut	99.51 %	99.54 %
Cumulative Efficiency	5.77 %	5.77 %

Table 2: Efficiency of the different preselection categories on the magnet up and magnet down polarity, together with the cumulative efficiency of all combined cuts on both samples. These efficiencies were derived from reconstructed signal Monte Carlo.

A short overview of the purpose of the preselection categories is given below:

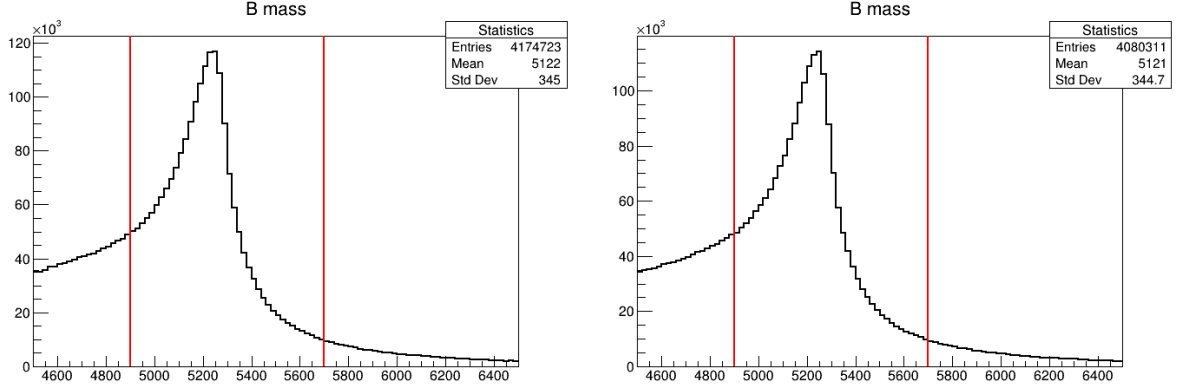
- **B Mass Cut:** The B mass cut serves to select signal B^0 (\bar{B}^0) mesons.
- **q^2 Cut:** The purpose of the q^2 cut is to select the phase space region where the decay happens via a on-shell J/ψ meson.
- **TriggerPresel:** Only select event that have the ‘*triggered on signal*’ tag.
- **MeerkatPresel ee:** Remove events with indecisive particle identification.
- **VetoPresel:** Remove various peaking backgrounds stemming from misidentified particles.
- **VetoPresel Bplus:** Remove contamination from B^+ (B^-) events.
- **PIDPresel ee:** Remove event for which particle identification was not stringent enough.
- **GenericPresel:** Select events that have Calorimeter and RICH information with them, and have a good χ^2 associated to their reconstructed tracks, together with a low ghost probability.
- **TighterKst0Presel:** Removes events for which the reconstructed K^{*0} mass differs by more than 100 MeV/c² from the PDG value [3].
- **BDT Cut:** Cut on the weight that is applied by a Boosted Decision Tree on how signal-like events are.

4.3.1 B mass, q^2 window and other kinematic cuts

The mass of the B^0 meson is given by the invariant mass of the four daughter particles. This invariant mass is determined by the `DecayTreeFitter` algorithm. The DTF uses the momenta of all particles in combination with the primary vertex (PV) to construct the B^0 mass:

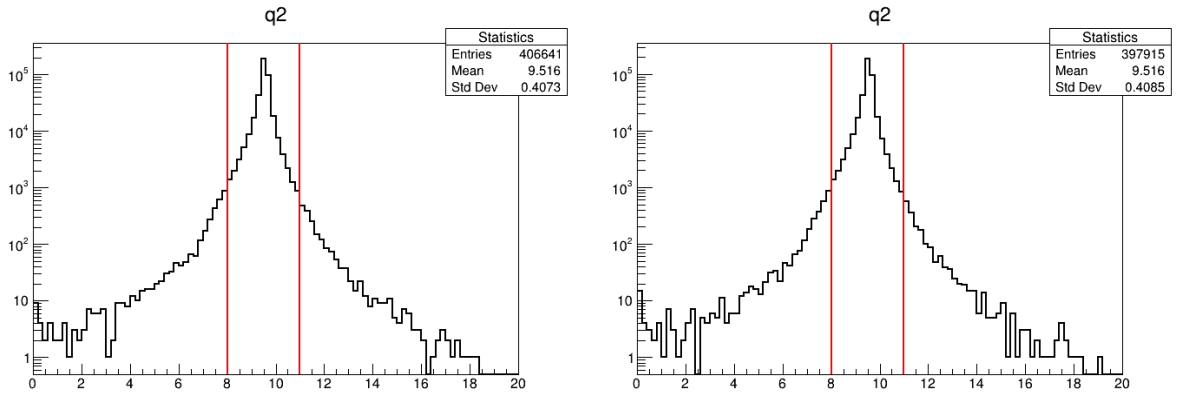
$$m(B^0) = m_{inv}(K^+\pi^-\mathrm{e}^-\mathrm{e}^+). \quad (22)$$

The mass of the B^0 is constrained to the range $[4900, 5700] \text{ MeV}/c^2$. All events with a reconstructed B^0 mass outside of this window are rejected. In order to select the events that decay via an on-shell J/ψ the invariant mass of the electron pair, q^2 , is cut around the nominal J/ψ mass. Therefore, we select events which have a q^2 in the range of $[8, 11] \text{ GeV}^2/c^4$, all events with a q^2 outside of this range are rejected. The q^2 variable we use for this is the `q2_PVandBDTF` variable that is PV and B mass constrained. After the B mass cut the combined efficiency of magnet up and magnet down cuts on q^2 is 75.85 %. In figure 16, we show the distribution of both the B mass and the dielectron invariant mass for a reconstructed signal Monte Carlo sample. The red lines represent the cuts we apply to these distributions. We reject all events that are not inside of the two red lines.



(a) B mass distribution of the magnet down sample before preselection.

(b) B mass distribution of the magnet up sample before preselection.



(c) q^2 distribution of the magnet down sample after preselection.

(d) q^2 distribution of the magnet up sample after preselection.

Figure 16: B mass and q^2 distributions of reconstructed signal MC. Cuts applied tot the samples are indicated by the red lines. All the events with a B mass or q^2 outside of the red lines were rejected.

The mass of the reconstructed K^{*0} is constrained to not be further than 100 MeV/ c^2 from the standard model value, as extracted from the Particle Data Group [3],

$$|m(K^{*0})_{DTF} - 895.55| < 100 \text{ MeV}/c^2 . \quad (23)$$

There are also cuts imposed on the transverse momentum of various particles. All events where the Kaon or Pion has a transverse momentum lower than 250 MeV are rejected. Events with an electron with transverse momentum lower than 500 MeV are also rejected.

4.3.2 Particle Identification cuts

Particle identification (PID) combines the information from different subdetectors to identify a given type of particle. Cuts are made on the variables associated to this PID process. In order to reject background from $K \leftrightarrow \pi$ misidentification, the cut

$$DLL_{K\pi}(K) > DLL_{K\pi}(\pi) \quad (24)$$

is applied. Here DLL stands for ‘difference of log-likelihood’ that is given by the difference of the two particle hypothesis log-likelihoods. To reject events where a proton is misidentified as a pion, the cuts

$$DLL_{p\pi}(\pi) > 0, \quad (25)$$

$$m_{K(\pi \rightarrow p)\mu\mu} \in [5575, 5665] \text{ MeV}/c^2, \quad (26)$$

are applied. These three cuts reject events such as $\Lambda_b^0 \rightarrow p K^- \mu^+ \mu^-$ where the proton is misidentified as pion.

4.3.3 Boosted Decision Tree

A Boosted Decision Tree (BDT) was trained to further differentiate between signal and background events. The BDT was trained on Monte Carlo samples and assigns a per event weight to represent how signal- or background- like an event is. The BDT was trained on the following variables:

- B_PT
- B_IPCHI2_OWNPV
- B_FDCHI2_OWNPV
- B_ENDVERTEX_CHI2
- B_DIRA_OWNPV
- B_DTF_PV_chi2_0
- Kstar_ENDVERTEX_CHI2
- Jpsi_ENDVERTEX_CHI2
- H_Min_PT
- H_Min_IPCHI2_OWNPV
- L_Max_PT
- L_Max_IPCHI2_OWNPV
- L_Min_PT
- L_Min_IPCHI2_OWNPV

Figure 17 shows the distribution of weights that was extracted from the Boosted Decision Tree for both the magnet up and magnet down polarities. The BDT cut that was applied to the data sample is $\text{BDT} > 0.99$. All events with a BDT value of less than 0.99 were rejected. This cuts had an efficiency of 41.261% for the magnet down polarity and an efficiency of 41.27% for the magnet up polarity. The BDT cut was the last cut that was applied in the preselection.

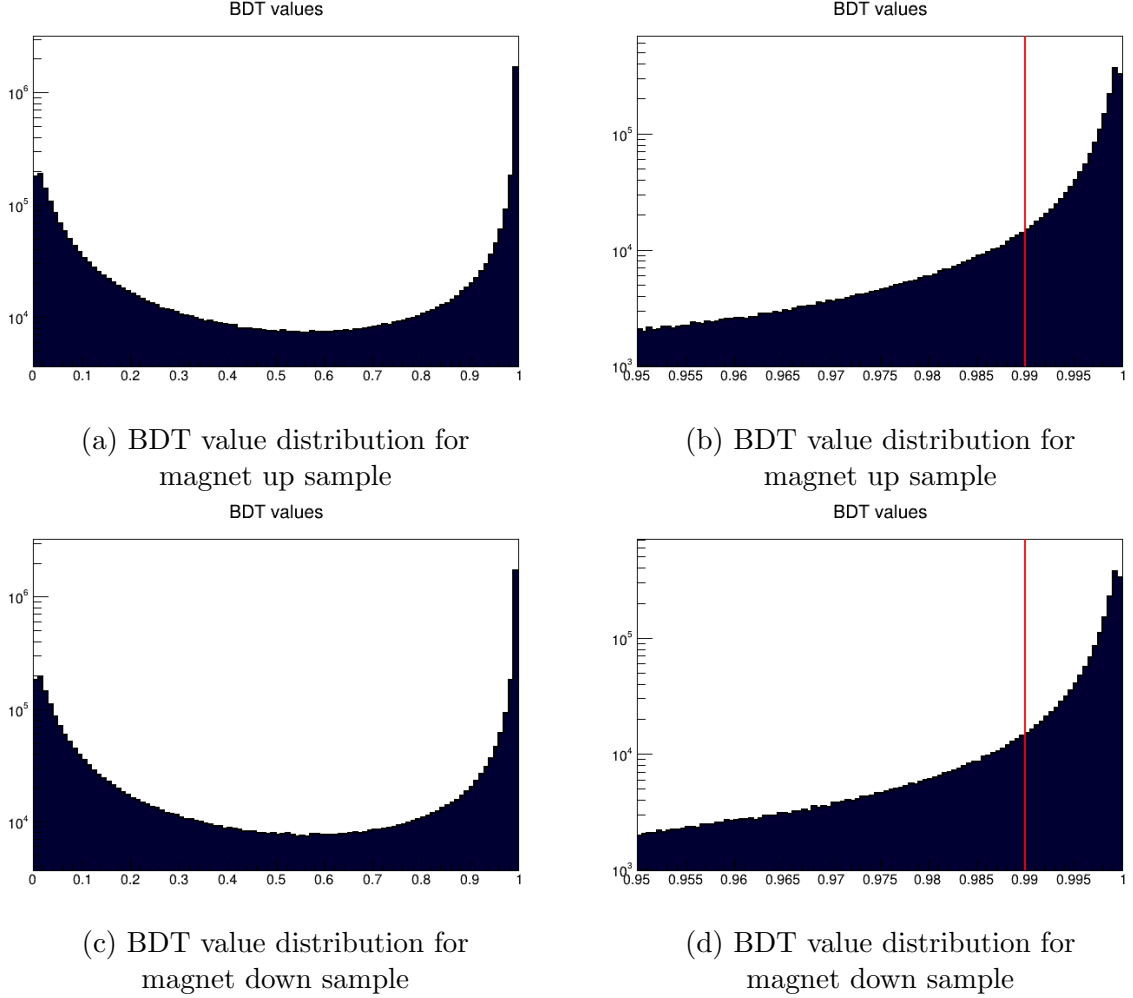


Figure 17: Distribution of values obtained from the Boosted Decision Tree for the data sample. The higher the value attached to the event the more signal-like the BDT deems the event. A cut was applied that removes all events with a BDT value under 0.99. The 0.99 value is indicated by the red line.

4.4 sWeights

In order to further distinguish between signal events and background events we make use of a technique called **sPlot** [22]. The purpose of this technique is to statistically separate signal and background distributions.

4.4.1 sPlot technique

In the **sPlot** technique the assumption is made that the distribution is characterized by variables of two types. The first set of components are the discriminating variables. They are the variables for which the distribution of signal events and background events is well known. The second set of variables are the control variables. The control variables are the variables for which the distributions are unknown. In the **sPlot** technique the essential assumption that is made is that the discriminating variable and control variable that are used are uncorrelated. We can formulate a naive weight for all events

$$\mathcal{P}_n(y_e) = \frac{N_n f_n(y_e)}{\sum_{k=1}^{N_s} N_k f_k(y_e)} , \quad (27)$$

with N_n the number of events expected for species n , where species are a type of event, e.g. background or signal. $f_n(y_e)$ represents the value of the PDF for species n with event e . Here N_s is the total number of species contained in the sample. One can construct the x -distribution from these weights by binning them in bins of x

$$N_n \tilde{M}_n(\bar{x}) \delta x \equiv \sum_{e \in \delta x} \mathcal{P}_n(y_e) , \quad (28)$$

where \tilde{M}_n represent the estimated distribution for x . This will, on average, produce the true distribution $\mathbf{M}_n(x)$. One average one can replace the above sum by the integral

$$\langle \sum_{e \in \delta x} \rangle \rightarrow \int dy \sum_{j=1}^{N_s} N_j f_j(x, y) \delta(x(y) - \bar{x}) \delta x . \quad (29)$$

By choosing our x and y such that they are uncorrelated, we can factorise the PDF $f_i(x, y)$ as $\mathbf{M}_i(x) f_i(y)$. If we then make the assumption that the expected number of events is the number of events as extracted from the fit we can rewrite equation 28 as

$$\begin{aligned} \langle N_n \tilde{M}_n(\bar{x}) \rangle &= \int \int dy dx \sum_{j=1}^{N_s} N_j \mathbf{M}_j(x) f_j(y) \delta(x - \bar{x}) \mathcal{P}_n \\ &= \int dy \sum_{j=1}^{N_s} N_j \mathbf{M}_j(\bar{x}) f_j(y) \frac{N_n f_n(y)}{\sum_{k=1}^{N_s} N_k f_k(y)} \\ &= N_n \sum_{j=1}^{N_s} \mathbf{M}_j(\bar{x}) \left(N_j \int dy \frac{f_n(y) f_j(y)}{\sum_{k=1}^{N_s} N_k f_k(y)} \right) . \end{aligned} \quad (30)$$

Here we see a correction term

$$N_j \int dy \frac{f_n(y) f_j(y)}{\sum_{k=1}^{N_s} N_k f_k(y)} . \quad (31)$$

This term is related to the inverse of the covariance matrix. The inverse of the covariance matrix is given by

$$\mathbf{V}_{nj}^{-1} = \sum_{e=1}^N \frac{f_n(y_e) f_j(y_e)}{(\sum_{k=1}^{N_s} N_k f_k(y_e))^2} . \quad (32)$$

If we take the average of this element and replace the sum by an integral using the definition given in equation 29 we get the relation

$$\begin{aligned} \langle \mathbf{V}_{nj}^{-1} \rangle &= \int \int dy dx \sum_{l=1}^{N_s} N_l \mathbf{M}_l(x) f_l(y) \frac{f_n(y) f_j(y)}{(\sum_{k=1}^{N_s} N_k f_k(y))^2} \\ &= \int dy \sum_{l=1}^{N_s} N_l f_l(y) \frac{f_n(y) f_j(y)}{(\sum_{k=1}^{N_s} N_k f_k(y))^2} \int dx \mathbf{M}_l(x) \\ &= \int dy \frac{f_n(y) f_j(y)}{\sum_{k=1}^{N_s} N_k f_k(y)} . \end{aligned} \quad (33)$$

Therefore we can replace the correction term that appeared in equation 30 by the term $\langle \mathbf{V}_{nj}^{-1} \rangle$, which gives us

$$\langle \tilde{M}_n(\bar{x}) \rangle = \sum_{j=1}^{N_s} \mathbf{M}_j(\bar{x}) N_j \langle \mathbf{V}_{nj}^{-1} \rangle . \quad (34)$$

If we invert the matrix equation we can construct the distribution of x as

$$N_n \mathbf{M}_n(\bar{x}) = \sum_{j=1}^{N_s} \langle \mathbf{V}_{nj} \rangle \langle \tilde{M}_j(\bar{x}) \rangle . \quad (35)$$

The associated weight is then called the sWeight and is defined as:

$${}_s\mathcal{P}_n(y_e) = \frac{\sum_{j=1}^{N_s} \mathbf{V}_{nj} f_j(y_e)}{\sum_{k=1}^{N_s} N_k f_k(y_e)} . \quad (36)$$

With this sWeight we can define the distribution of our control variable x as

$$N_n \tilde{M}_n(\bar{x}) \delta x \equiv \sum_{e \in \delta x} \mathcal{P}_n(y_e) , \quad (37)$$

which will on average reproduce the true distribution:

$$\langle N_n \tilde{M}_n(x) \rangle = N_n \mathbf{M}_n(x) . \quad (38)$$

4.4.2 Implementation of sWeights

In this analysis we want to differentiate signal and background events in the distribution of the angles θ_K , θ_l and ϕ . Within the `sPlot` framework these will be our control variables. We need to select a discriminating variable on which to fit in order to extract sWeights. This variable needs to be uncorrelated to the three angles and the distribution of this variable has to be well known in order to construct a proper fitting model. The variable we choose to fit for extracting the sWeights is the reconstructed mass of the B meson. We expect the correlation with this variable to be small. The distribution of the

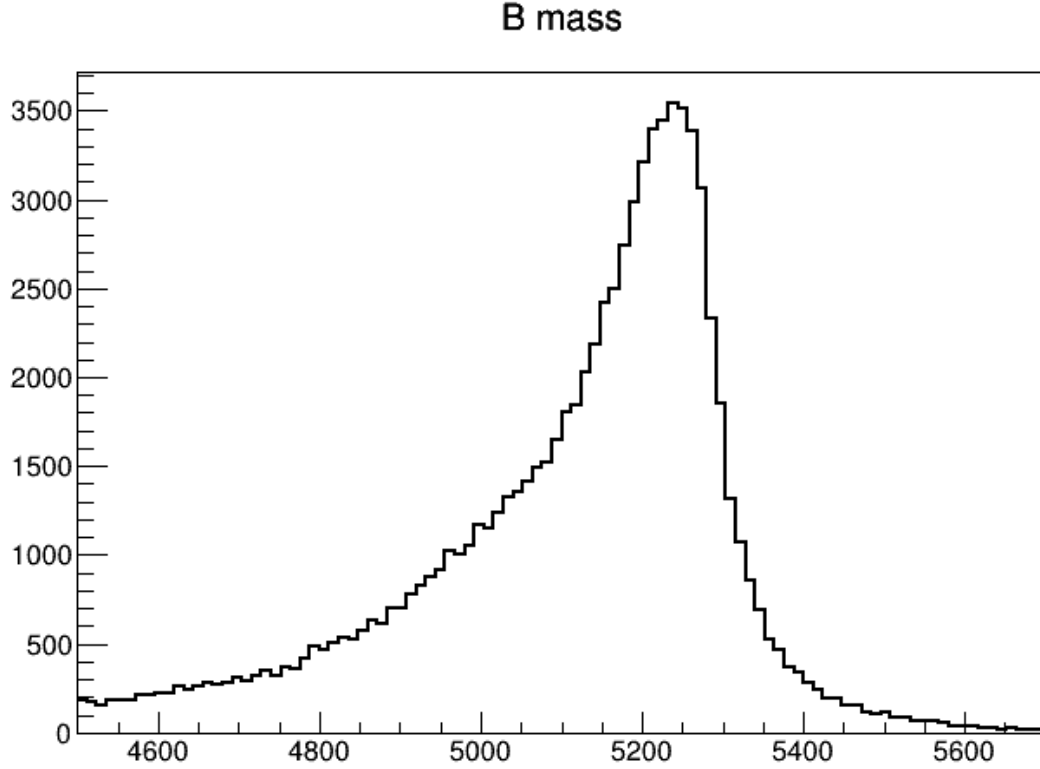


Figure 18: The mass distribution of the B meson for the data sample used in this analysis after preselection. We will use this distribution to extract sWeights by fitting signal and background components.

B meson mass is given in figure 18. We need to construct PDFs that are used in fitting the signal and background component. For modelling the background we have chosen to use an exponential function. The exponential function is sufficient as there are no large peaking backgrounds in the sample due to the various cuts that were applied before fitting the sample. The background therefore consists mainly of combinatorial background. This is background stemming from random combinations of particles that can be reconstructed as our signal candidate. The exponential function is given by $\mathcal{N} \cdot e^{c \cdot x}$, with \mathcal{N} a normalisation constant dependant on the range and values of the arguments. For modelling the signal events we use the sum of two Crystal Ball functions. This function is named after the Crystal Ball Collaboration and consists of a Gaussian core with one of the sides modelled as a power-law from a certain threshold. The Crystal Ball function is defined as [23]:

$$f(x, \alpha, n, \bar{x}, \sigma) = N \cdot \begin{cases} \exp\left(-\frac{(x - \bar{x})^2}{2\sigma^2}\right), & \text{for } \frac{x - \bar{x}}{\sigma} > -\alpha, \\ A \cdot \left(B - \frac{x - \bar{x}}{\sigma}\right)^{-n}, & \text{for } \frac{x - \bar{x}}{\sigma} \leq -\alpha, \end{cases} \quad (39)$$

with

$$\begin{aligned}
A &= \left(\frac{n}{|\alpha|} \right)^n \cdot \exp\left(-\frac{|\alpha|^2}{2} \right), \\
B &= \frac{n}{|\alpha|} - |\alpha|, \\
N &= \frac{1}{\sigma(C + D)}, \\
C &= \frac{n}{|\alpha|} \cdot \frac{1}{n-1} \cdot \exp\left(-\frac{|\alpha|^2}{2} \right), \\
D &= \sqrt{\frac{\pi}{2}} \left(1 + \operatorname{erf}\left(\frac{|\alpha|}{\sqrt{2}} \right) \right).
\end{aligned} \tag{40}$$

Here erf is the error function and α , n , \bar{x} and σ are the fit parameters. We choose the two Crystal Ball functions in our fit model to have power tails on opposite sides. In the fit they share the parameter \bar{x} which determines the mean of the Gaussian distribution. This parameter corresponds to the mean value of the B meson mass distribution. The value F_l represent the fraction of the Crystal Ball function with a power tail on the left, in the sum of the two Crystal Ball functions. The values of the parameters extracted from the fit are given in table 3 with the resulting fit of the B meson mass shown in figure 19. The distribution of signal and background weights for the events are shown in figure 20.

Parameter	Fitted value
F_l	81.967 %
\bar{x}	5.2435×10^3
α_l	2.1185×10^{-1}
α_r	-3.7262×10^0
n_l	1.0751×10^2
n_r	7.7334×10^1
σ_l	4.2973×10^1
σ_r	1.1738×10^2
c	-9.3763×10^{-4}

Table 3: Parameters extracted by fitting the B meson mass distribution using two Crystal Ball shapes for the signal component and an exponential function for the background component.

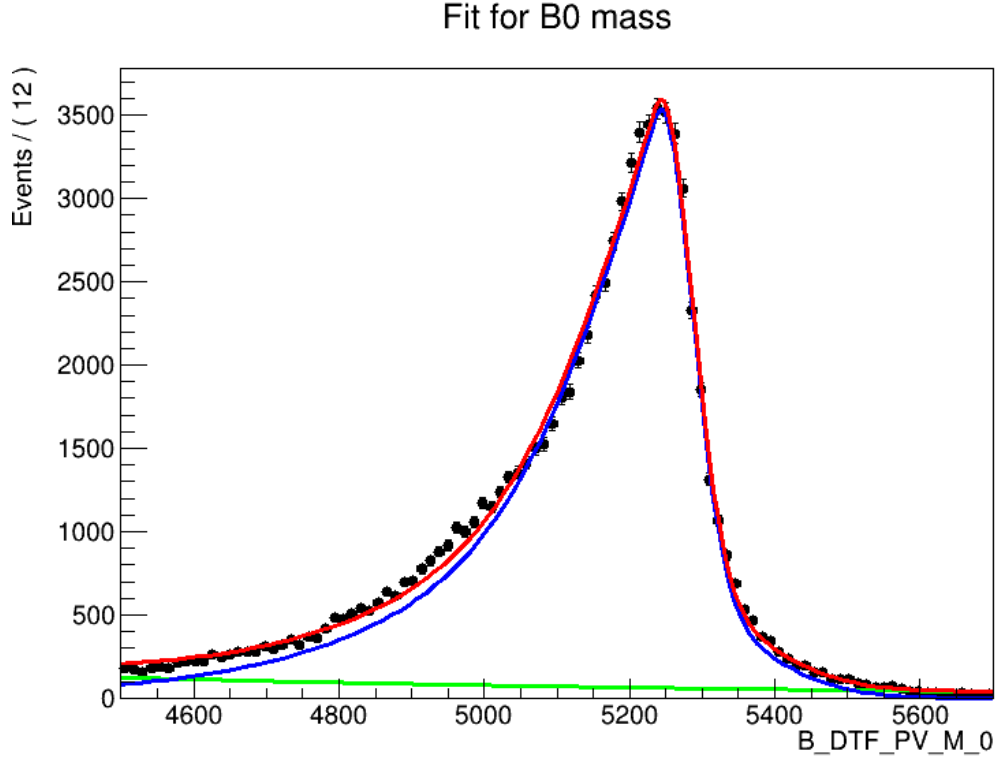


Figure 19: Fit on the B^0 mass distribution for the data sample that was used in this analysis shown in red. This fit was used to extract sWeights. The background is modelled by an exponential function (green). The signal peak is modelled by two Crystal Ball functions (blue). The function does not fit the distribution very well. Because we have a large signal to background ratio due to the various cuts that are applied, this will have a limited effect on our final results.

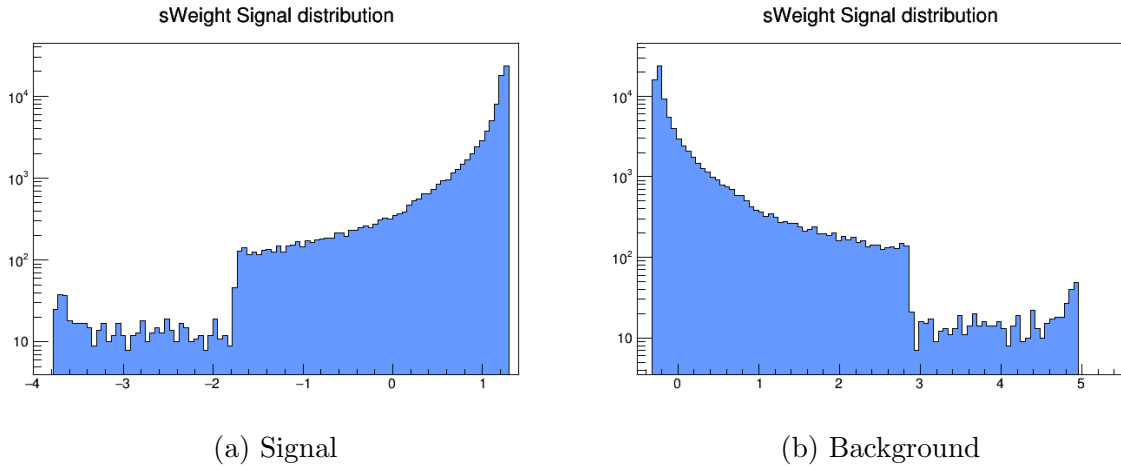


Figure 20: For the data sample used in this analysis are shown: (a) Distribution of signal sWeights. (b) Distribution of background sWeights. These values are later used in a weighted fit of the angular distributions.

5 Fit Framework

The fitting framework that is being used to run the angular fit is called **Ipanema** [24]. It is a framework that utilises Graphics Processing Units (GPU). This enables a large gain in computing speed as it facilitates parallel processing. This is especially useful in particle physics as analysis often rely on processing large data samples. By adapting the software to make use of the parallel capabilities of GPUs computing time can be greatly reduced. The fitter is written in CUDA and interfaces with **pyCUDA** [25]. The minimiser that is used in fitting is **iMinuit** [26], which is a Python front end to the C++ **MINUIT2** [27] package that runs on the CPU. The per-event log-likelihood is computed on the GPU. **MINUIT** [28] is a physics analysis tool that can minimise user defined functions and is often used for likelihood fits.

5.1 Validating the Fitter

In order to validate the results extracted from the fitter we fitted a generator level signal Monte Carlo (MC) sample containing 475k events. Generator level samples are created directly from physics PDF's and do not contain detector effects. The PDF that is used for generating the sample is known a priori. This makes it an ideal candidate to test the fitting of the angular distributions given by the PDF, without the modification from detector acceptance. The parameters extracted from the fit should be in agreement with the parameters that were used to generate the sample.

5.1.1 Extracting the PDF parameters

The Monte Carlo sample that is used in validating the fitter is generated using helicity amplitudes H_0 , H_+ and H_- , according to the Jacob-Wick convention [29]. The angular distribution is generated with only contributions from the P-wave K^{*0} system. This means that all parameters related to the S-wave are zero. To compare these values to the values extracted from the fit they need to be converted to the angular observables used in this analysis. One can do this using the definitions given in [30], relating the helicity amplitudes to the decay amplitudes as

$$A_{\perp,\parallel} = (H_+ \mp H_-)/\sqrt{2}, \quad A_0 = H_0. \quad (41)$$

In generating the Monte Carlo sample the left handed chirality and the right handed chirality transversity amplitudes were set to be equal and the amplitudes A_t and A_s were set to be zero. Using the relations in equation 7 we can calculate the angular observables by substituting the values used in generating the Monte Carlo sample as

$$\begin{aligned} A_{\perp}^L &= A_{\perp}^R = \frac{1}{2}A_{\perp} = \frac{1}{2\sqrt{2}}(H_+ - H_-), \\ A_{\parallel}^L &= A_{\parallel}^R = \frac{1}{2}A_{\parallel} = \frac{1}{2\sqrt{2}}(H_+ + H_-), \\ A_0^L &= A_0^R = \frac{1}{2}A_0 = \frac{1}{2}H_0. \end{aligned} \quad (42)$$

We can then use equation 8 to calculate the angular observables to which to compare our fit results. The helicity amplitude values that were used in generating our Monte Carlo sample for H_0 , H_+ and H_- are

$$\begin{aligned}
H_0 &= 0.775e^{0i}, \\
H_+ &= 0.159e^{1.563i}, \\
H_- &= 0.612e^{2.712i}.
\end{aligned}
\tag{43}$$

These values are based on values published by the Babar collaboration. In table 4 the angular observables calculated from these helicity amplitudes are given together with a fit to the Monte Carlo sample.

5.1.2 Fitting generator level Monte Carlo

The fit projections of the three angles are shown in figure 21. The values obtained from this fit are given in table 4. Table 5 shows the correlation between the different parameters in the fit. When we compare the values extracted from the fit to the values used in generating the sample we find a good agreement in with most parameters matching within the given statistical error range. This validates the implementation of the PDF inside of the fitter, and shows us the minimisation of the log-likelihood is functioning properly.

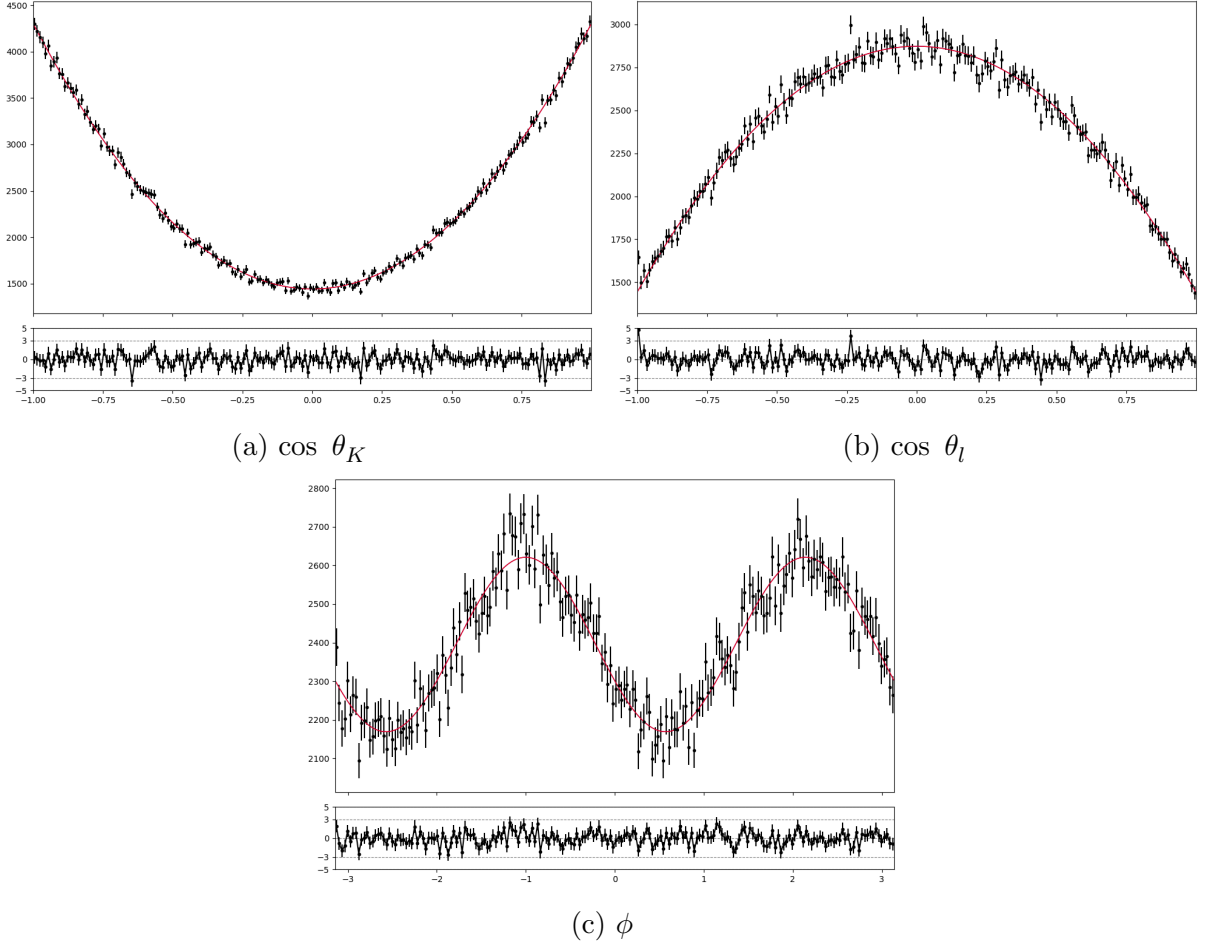


Figure 21: Fit projections obtained from fitting a generator level signal Monte Carlo sample containing ~ 475 k events after preselection.

Parameter	Generator value	Fit value	Stat. error
F_L	0.6003	0.5988	± 0.0010
S_3	-0.0398	-0.0394	± 0.0014
S_4	-0.2150	-0.2186	± 0.0015
S_5	0	0.0028	± 0.0015
A_{FB}	0	-0.0006	± 0.0010
S_7	0	-0.0007	± 0.0016
S_8	0.0371	0.0388	± 0.0016
S_9	-0.0887	-0.0860	± 0.0014

Table 4: Table showing the values used in generating the signal Monte Carlo sample and the values extracted from fitting the angular distributions of the sample.

	F_L	S_3	S_4	S_5	A_{FB}	S_7	S_8	S_9
F_L	1.00	0.05	0.05	0.00	0.00	0.00	-0.01	0.09
S_3		1.00	-0.09	0.00	0.00	0.00	-0.01	-0.01
S_4			1.00	0.00	0.00	0.00	-0.02	0.00
S_5				1.00	-0.16	-0.05	0.00	0.00
A_{FB}					1.00	0.02	0.00	0.00
S_7						1.00	0.00	0.00
S_8							1.00	-0.08
S_9								1.00

Table 5: Table showing the correlations obtained fitting the generator level signal Monte Carlo sample.

5.1.3 Pseudo-experiments

In order to check the consistency of the fitter we ran a toy study. In this toy study we generated 1000 data samples according to the PDF parameters we extracted from fitting the generator level sample found in table 4. We then fitted these 1000 samples and compared the extracted fit parameters with the ones that were used in generating the samples. We binned the difference between the fitted toy parameter and the parameter used in generating the toy, divided by the estimated error, in a histogram. This is commonly called the pull. The resulting distribution was then fitted with a Gaussian function. These fits are shown in figure 22. In order for the fit to be stable, the resulting means of the parameter should not differ significantly from 0 and the sigmas should approach 1 for a large sample of toys for the fit to be stable. This was also the behaviour that was found while performing the toy study.

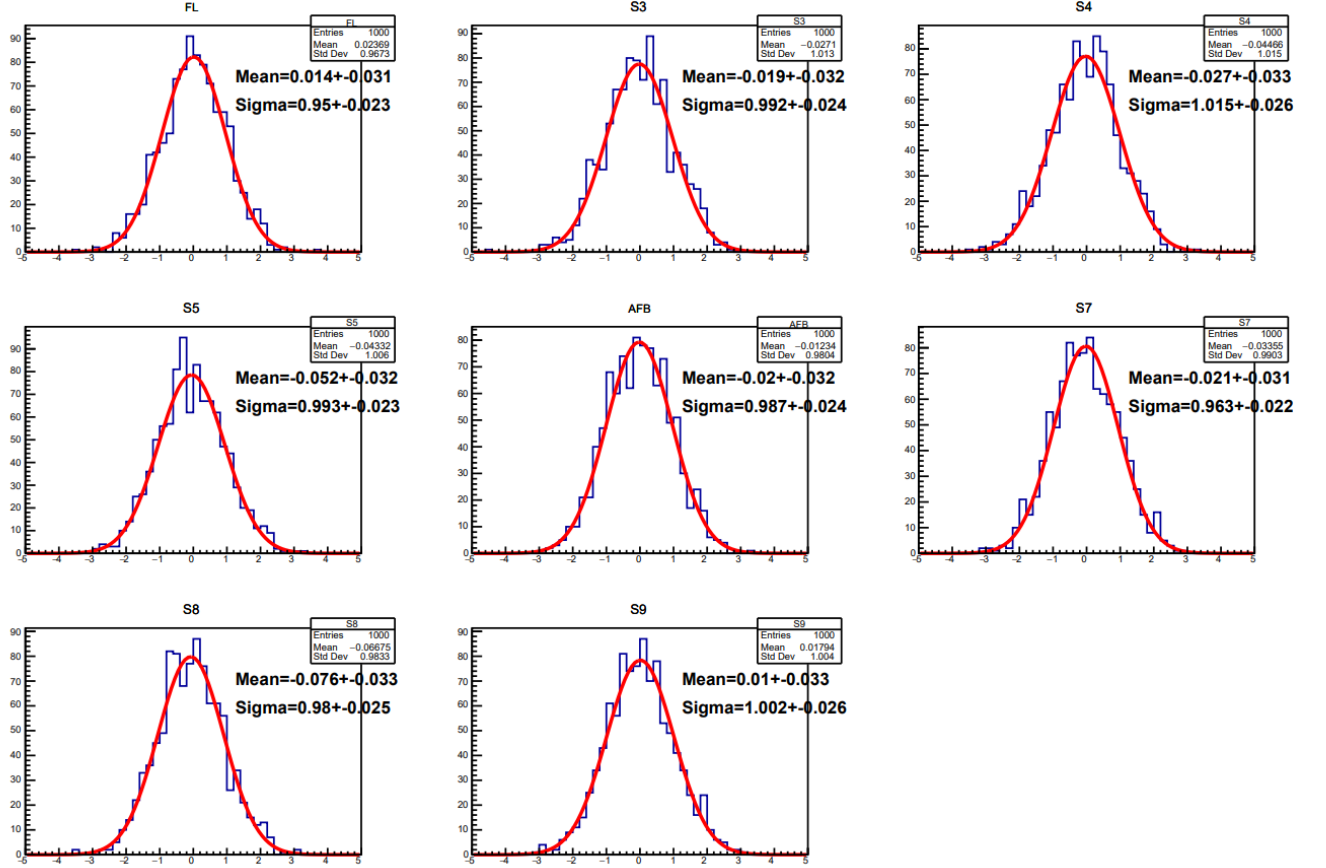


Figure 22: Parameter pull distributions obtained by a toy study done on 1000 toys generated using the parameters extracted from the generator level Monte Carlo sample. The pulls of fitting the toys were fitted with a Gaussian function. The extracted distributions of fit values show a good agreement with a Gaussian function with mean 0 and sigma 1. This indicates stable fitting.

5.1.4 Fitting reconstructed Monte Carlo

After fitting a generator level signal sample to validate fitting the physics PDF we proceed to analyse a reconstructed signal Monte Carlo sample. Reconstructed Monte Carlo samples generate events and then simulate detector effects. In order to validate the acceptance parametrisation used in the fitter we fit the reconstructed sample. The fit projections of the angular distributions of the reconstructed Monte Carlo sample are shown in figure 23. Here the blue line represents the fitted product of the PDF and the acceptance divided by the proper normalisation. The red line represents the *raw* associated PDF. In figure 23(a) we can see that the fit can properly account for the distribution going to zero for $\cos \theta_k$ going to 1. This means that the order we used in parametrising the detector acceptance was adequate for describing the rapid declining detector efficiency in that region of phase space. Another interesting aspect is the shift in the phi distribution introduced by the detector efficiency that can be seen in figure 23(c). The values for the angular observables extracted from the fit are given in table 6. Table 7 shows the correlation of the fit parameters.

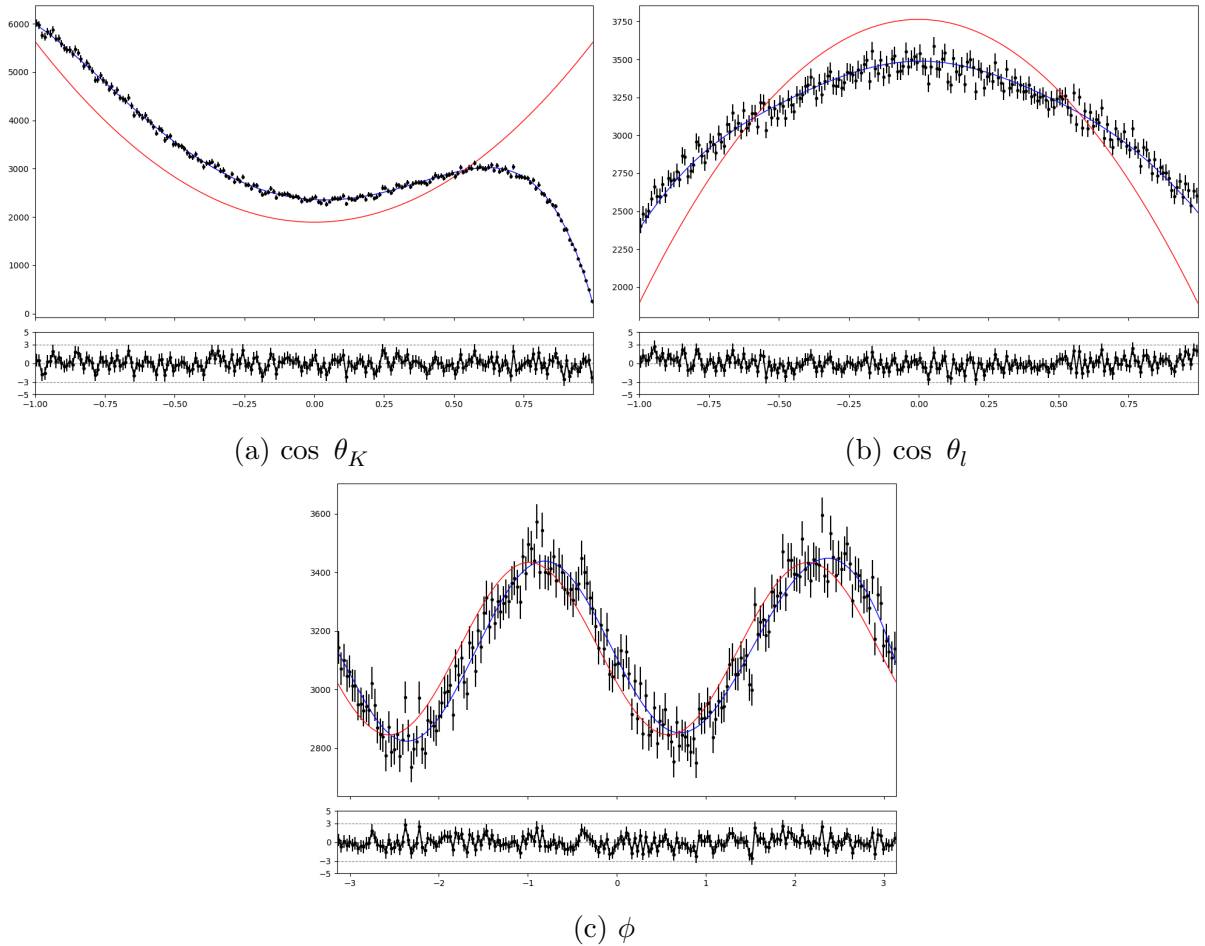


Figure 23: Fit projections obtained from fitting a reconstructed signal Monte Carlo sample containing $\sim 627k$ events after preselection. Here the blue line represent the fit on the distribution using an acceptance parametrisation that modifies the PDF. The red line represent the resulting *raw* PDF that is unmodified by detector effects.

Most values extracted from the fit show a good agreement with the values used in generating the sample. However, the fit of the reconstructed Monte Carlo sample does not statistically agree with the generated values as well as the fit of the generator Monte Carlo sample did. As shown in section 3.3.2, we can see small deviations in the projections of the acceptance parametrisation and the true acceptance. It is not clear that this would cause the deviation observed when comparing the fit to the reconstructed and generator level Monte Carlo samples. The effect and origin of this deviation is not well understood, and should be studied further in future analyses.

Parameter	Generator value	Rec. Sample	Gen. Sample
F_L	0.60035	0.5981 ± 0.0008	0.5988 ± 0.0010
S_3	-0.03981	-0.0369 ± 0.0011	-0.0394 ± 0.0013
S_4	-0.2150	-0.2464 ± 0.0012	-0.2186 ± 0.0015
S_5	0	0.0000 ± 0.0012	0.0027 ± 0.0015
A_{FB}	0	-0.0003 ± 0.0007	-0.0006 ± 0.0009
S_7	0	0.0008 ± 0.0013	-0.0006 ± 0.0015
S_8	0.03714	0.0393 ± 0.0013	0.0388 ± 0.0016
S_9	-0.08873	-0.0862 ± 0.0011	-0.0859 ± 0.0013

Table 6: Values from fitting the reconstructed signal Monte Carlo sample. This reconstructed Monte Carlo sample was generated from the same PDF as the generator level Monte Carlo sample fitted before. The fit results obtained from fitting the generator level signal Monte Carlo sample are also shown.

	F_L	S_3	S_4	S_5	A_{FB}	S_7	S_8	S_9
F_L	1.00	0.05	0.09	0.00	0.00	0.00	-0.02	0.10
S_3		1.00	-0.11	0.00	0.00	0.00	-0.01	-0.02
S_4			1.00	0.00	0.00	0.00	-0.02	0.01
S_5				1.00	-0.18	-0.05	0.00	0.00
A_{FB}					1.00	0.02	0.00	0.00
S_7						1.00	0.00	0.00
S_8							1.00	-0.10
S_9								1.00

Table 7: Table showing the correlation of fit parameters in the reconstructed signal Monte Carlo sample fit.

6 Results

When fitting the data sample we found a good agreement between the angular projections extracted from the fit and the data distributions. The data distributions are shown together with the angular projections extracted from the fit for: $\cos \theta_K$ in figure 24, $\cos \theta_l$ in figure 25 and ϕ in figure 26. The blue line represents the angular projection of the extracted PDF as modified by the detector acceptance. The red line represents the associated *raw* PDF, unmodified by detector acceptance. We can see that the blue line closely follows the data distribution, with the pulls showing no distinct trend. Table 8 shows the values as extracted from the fit. The S-wave component of the PDF accounts for $\sim 12\%$ of the distribution. A table giving the correlation of the fit parameters is given in table 9.

Parameter	Fitted value	Stat. error
F_L	0.5986	± 0.0035
S_3	-0.0068	± 0.0050
S_4	-0.2883	± 0.0046
S_5	-0.0036	± 0.0052
A_{FB}	0.0097	± 0.0030
S_7	-0.0044	± 0.0057
S_8	-0.0362	± 0.0055
S_9	-0.0846	± 0.0051
F_S	0.1224	± 0.0070
S_{11}	-0.0385	± 0.0079
S_{13}	0.0784	± 0.0085
S_{14}	-0.0146	± 0.0037
S_{15}	-0.0012	± 0.0035
S_{16}	-0.0054	± 0.0037
S_{17}	-0.0360	± 0.0040

Table 8: Angular observables extracted from fitting the data sample.

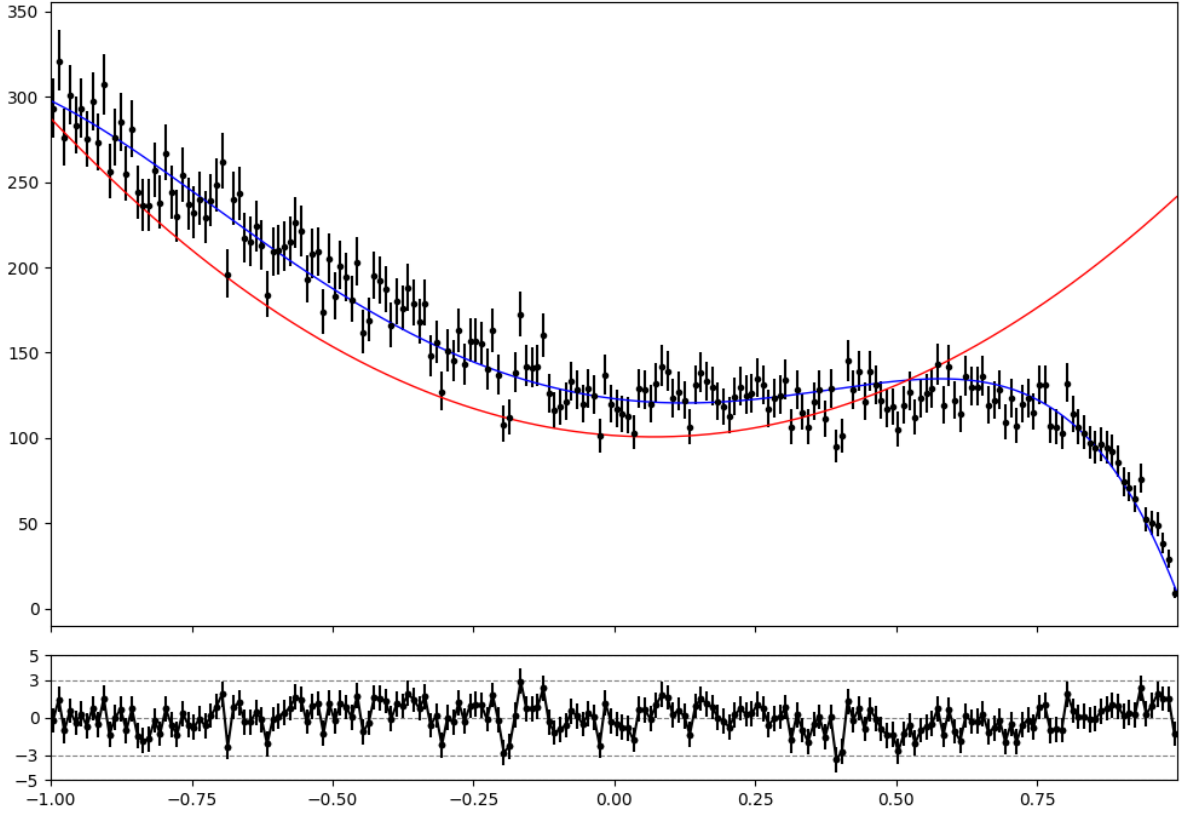


Figure 24: Angular projection of the $\cos \theta_K$ angle obtained from fitting the data sample containing 31165 events. Here the blue line represent the fit on the distribution using an acceptance parametrisation that modifies the PDF. The red line represent the resulting *raw* PDF that is unmodified by detector effects.

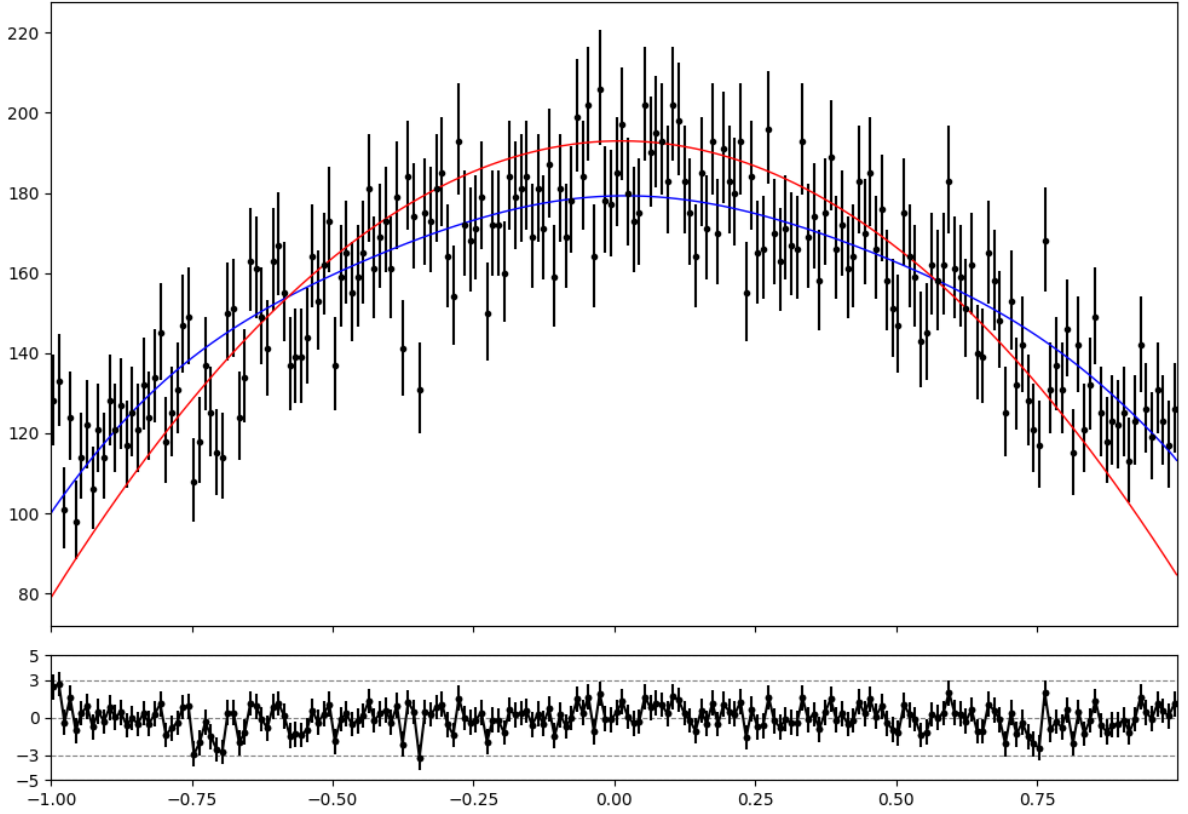


Figure 25: Angular projection of the $\cos \theta_l$ angle obtained from fitting the data sample containing 31165 events. Here the blue line represent the fit on the distribution using an acceptance parametrisation that modifies the PDF. The red line represent the resulting *raw* PDF that is unmodified by detector effects.

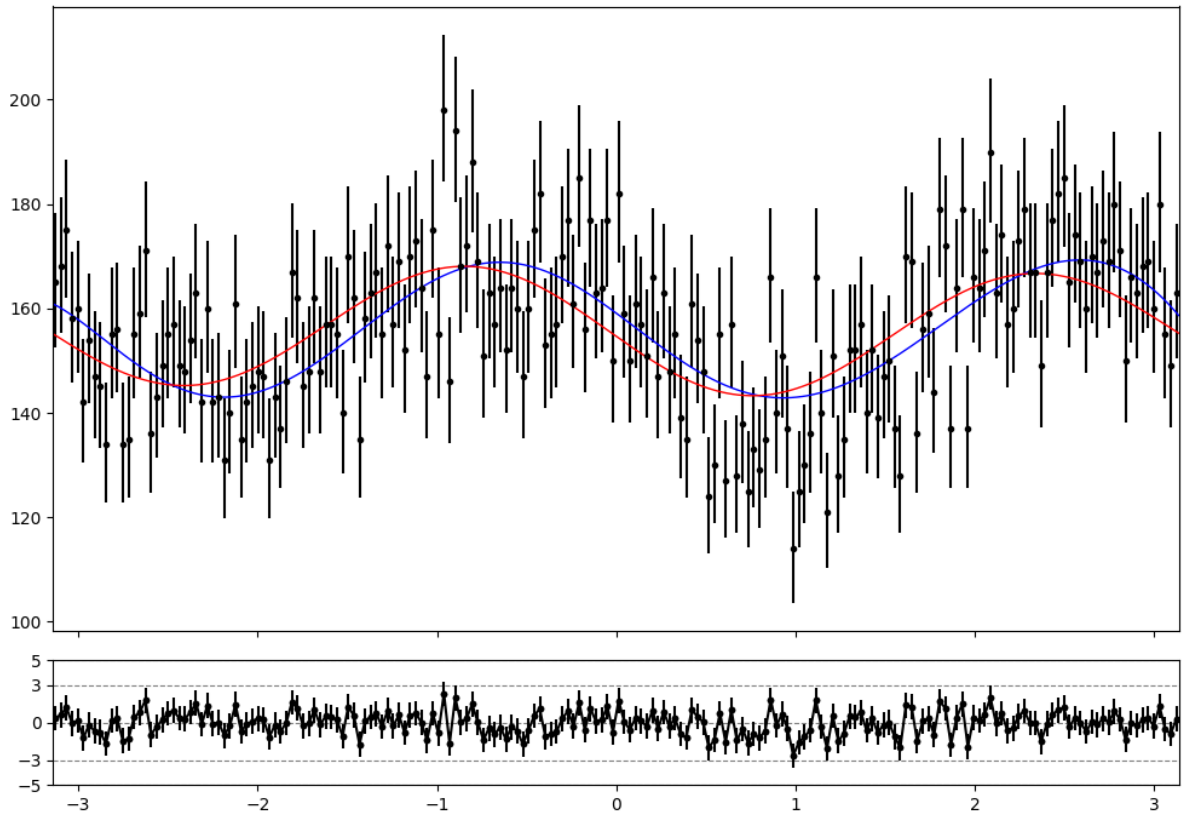


Figure 26: Angular projection of the ϕ angle obtained from fitting the data sample containing 31165 events. Here the blue line represent the fit on the distribution using an acceptance parametrisation that modifies the PDF. The red line represent the resulting *raw* PDF that is unmodified by detector effects.

	F_L	S_3	S_4	S_5	A_{FB}	S_7	S_8	S_9	F_S	S_{11}	S_{13}	S_{14}	S_{15}	S_{16}	S_{17}
F_L	1.00	0.00	0.09	-0.03	-0.04	-0.01	0.01	0.03	0.09	0.23	-0.21	-0.07	0.01	0.00	0.01
S_3		1.00	-0.06	-0.01	0.00	0.00	0.01	0.00	-0.03	-0.03	0.03	-0.01	0.00	0.01	0.02
S_4			1.00	0.07	0.06	0.01	-0.06	0.01	-0.20	0.03	-0.02	0.08	-0.05	-0.01	-0.01
S_5				1.00	-0.17	-0.05	0.01	0.0	-0.02	-0.01	0.01	-0.05	0.03	-0.01	-0.01
A_{FB}					1.00	-0.03	0.02	0.00	0.00	-0.03	0.03	-0.03	0.00	-0.03	-0.01
S_7						1.00	0.01	0.00	-0.01	-0.01	0.00	-0.01	-0.01	0.03	-0.01
S_8							1.00	-0.07	-0.02	-0.06	0.07	0.1	-0.01	-0.01	0.06
S_9								1.00	-0.15	0.01	-0.01	-0.03	-0.01	0.00	-0.02
F_S									1.00	-0.11	0.10	0.02	0.00	-0.01	0.00
S_{11}										1.00	-1.00	-0.28	-0.01	-0.01	-0.05
S_{13}											1.00	0.28	0.01	0.01	0.04
S_{14}												1.00	0.02	0.01	-0.05
S_{15}													1.00	-0.06	0.00
S_{16}														1.00	0.00
S_{17}															1.00

Table 9: Table showing the correlations obtained fitting the data sample.

7 Conclusion

In this analysis the angular observables describing the angular distributions of the $B^0 \rightarrow K^{*0} J/\psi (\rightarrow e^+ e^-)$ decay were determined from a fit. The data sample that was used in this analysis is the data gathered by the LHCb detector in the year 2016 and corresponds to a total integrated luminosity of 1.665 fb^{-1} at a total centre-of-momentum energy of 13 TeV. No systematic errors were determined in this analysis. The decay that is analysed in this thesis is part of the analyses that are being done by the LHCb collaboration that test lepton universality. Results by the LHCb collaboration show a 2.5σ tension [6] with the lepton universality assumption in the Standard Model. The $B^0 \rightarrow K^{*0} J/\psi (\rightarrow \ell^+ \ell^-)$ decays play a role in the analysis of the \mathcal{R}_K^* variable, where they serve as control channels. Because the $B^0 \rightarrow K^{*0} J/\psi (\rightarrow \ell^+ \ell^-)$ decay results in the same final state as the rare decay $B^0 \rightarrow K^{*0} \ell^+ \ell^-$ it is also a good test of how well the detector is understood. The $B^0 \rightarrow K^{*0} \ell^+ \ell^-$ decay with final state muons has been extensively studied by the LHCb collaboration [7, 8, 9]. Final state electrons are however more difficult to analyse in the LHCb detector. Leptons undergo bremsstrahlung due to their interaction with the Coulomb field of the atoms that make up the detector. Because this interaction scales with the mass of the leptons the electrons are more affected by this effect.

Parameter	2016 electron fit	2016 muon fit
F_L	0.5986 ± 0.0035	0.5643 ± 0.0014
S_3	-0.0068 ± 0.0050	-0.0008 ± 0.0018
S_4	-0.2883 ± 0.0046	-0.2459 ± 0.0020
S_5	-0.0036 ± 0.0052	0.0035 ± 0.0020
A_{FB}	0.0097 ± 0.0030	0.0005 ± 0.0012
S_7	-0.0044 ± 0.0057	0.0017 ± 0.0020
S_8	-0.0362 ± 0.0055	-0.0573 ± 0.0021
S_9	-0.0846 ± 0.0051	-0.0844 ± 0.0018
F_S	0.1224 ± 0.0070	0.0586 ± 0.0022
S_{11}	-0.0385 ± 0.0079	-0.1104 ± 0.0018
S_{13}	0.0783 ± 0.0085	0.1104 ± 0.0018
S_{14}	-0.0146 ± 0.0037	0.0214 ± 0.0023
S_{15}	-0.0012 ± 0.0035	-0.0013 ± 0.0021
S_{16}	-0.0054 ± 0.0037	-0.0007 ± 0.0022
S_{17}	-0.0360 ± 0.0040	-0.0655 ± 0.0024

Table 10: Angular observables extracted from fitting the 2016 electron sample together with the angular observables extracted as part of the angular analysis done by the LHCb collaboration on the $B^0 \rightarrow K^{*0} \mu^+ \mu^-$ decay [7]. The angular observables for the muon on-shell J/ψ mode are from internal LHCb documentation as they serve as a control channel in the $B^0 \rightarrow K^{*0} \mu^+ \mu^-$ decay.

A recent analysis by LHCb was the angular analysis of the $B^0 \rightarrow K^{*0} e^+ e^-$ decay in the low q^2 region [4], where q^2 is the invariant mass of the lepton pair. This thesis is part of the effort to extend the q^2 range over which the angular analysis is done, to further improve the understanding of leptons and their role in the Standard Model. The angular observables obtained from the fit of the $B^0 \rightarrow K^{*0} J/\psi (\rightarrow \ell^+ \ell^-)$ decay with final state electrons are given in table 10. They are accompanied by the angular observables that were determined from the muon final state during the latest $B^0 \rightarrow K^{*0} \mu^+ \mu^-$ analysis done

by LHCb [7]. The values of the angular observables for the muon final state are taken from internal LHCb documentation as they serve as a control sample, and are therefore not included in the final paper. Figure 27 shows the difference between the electron and muon channel per angular observable, divided by the value of the electron observable.

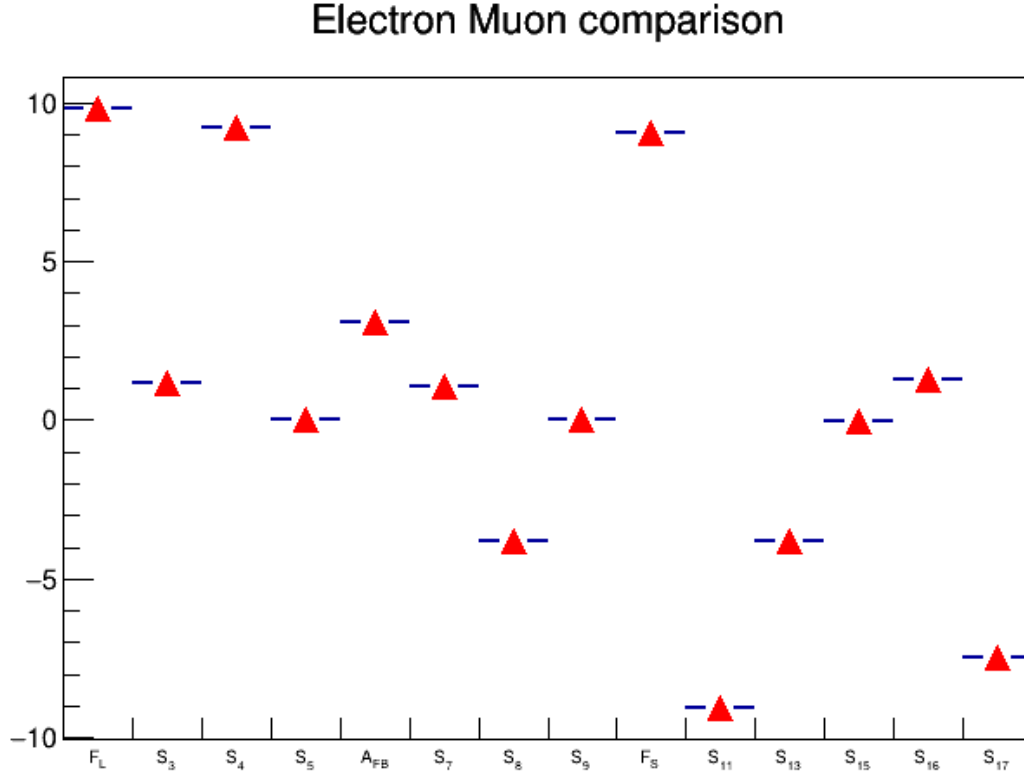


Figure 27: Difference between the angular observables for the decays $B^0 \rightarrow K^{*0} J/\psi (\rightarrow \ell^+ \ell^-)$ with electron and muon final states divided by the electron error. The electron observables were extracted from a fit that is part of this thesis. The muon observables were taken from internal documentation describing the rare decay analysis.

The fit result for the electron final state obtained in this thesis is statistically incompatible with the fit results for the muon final state as obtained during a previous LHCb analysis. A possible cause of this deviation can be seen in figure 15, where the projections of the acceptance parametrisation used in this thesis are shown. The acceptance parametrisation projections show small deviations from the true acceptance. Because these deviations are small their effect on the final parameters extracted from the fit are unclear. More effort is needed to study this effect. This analysis also lacks an extensive study of the angular behaviour of background components. The angular contributions stemming from the B_s^0 meson were not properly disentangled from the B^0 distributions. Instead the angular behaviour of the B_s^0 was assumed to be identical to the B^0 . The sWeight model used to statistically separate background and signal distributions is also lacking fidelity. With the further improvement of parts of this analysis, the fit results for the electron sample could potentially come to better agreement with the results obtained from the muon fit. However, the results obtained in this analysis are a strong proof of concept of the analysis method that was employed in this thesis.

References

- [1] J. Tuominiemi. Search for the top quark in UA1 and in the other hadron collider experiments. *Acta Phys. Polon. B*, 21:327–343, 1990.
- [2] Stephen King. Discrete symmetries and models of flavour mixing. *Journal of Physics: Conference Series*, 631:012005, 07 2015.
- [3] M. et al. Tanabashi. Review of particle physics. *Phys. Rev. D*, 98:030001, Aug 2018.
- [4] The LHCb Collaboration. Angular analysis of the $B^0 \rightarrow K^{*0} e^+ e^-$ decay in the low- q^2 region, 2015.
- [5] Simone Bifani, Sébastien Descotes-Genon, Antonio Romero Vidal, and Marie-Hélène Schune. Review of lepton universality tests in B decays. *Journal of Physics G: Nuclear and Particle Physics*, 46(2):023001, Dec 2018.
- [6] The LHCb Collaboration. Test of lepton universality with $B^0 \rightarrow K^{*0} \ell^+ \ell^-$ decays. *JHEP*, 08:055, 2017.
- [7] The LHCb Collaboration. Measurement of CP-Averaged Observables in the $B^0 K^{*0} \mu^+ \mu^-$ Decay. *Physical Review Letters*, 125(1), Jul 2020.
- [8] The LHCb Collaboration. Angular analysis of the $B^0 \rightarrow K^{*0} \mu^- \mu^+$ decay using 3 fb^{-1} of integrated luminosity. *Journal of High Energy Physics*, 2016(2), Feb 2016.
- [9] The LHCb Collaboration. Differential branching fraction and angular analysis of the decay $B^0 \rightarrow K^{*0} \mu^+ \mu^-$. *JHEP*, 08:131, 2013.
- [10] The LHCb Collaboration. The LHCb Detector at the LHC. *JINST*, LHCb.
- [11] The ATLAS collaboration. The ATLAS Experiment at the CERN Large Hadron Collider. *JINST*, 3:S08003, 2008.
- [12] The CMS collaboration. The CMS Experiment at the CERN LHC. *JINST*, 3:S08004, 2008.
- [13] The ALICE collaboration. The ALICE experiment at the CERN LHC. *JINST*, 3:S08002, 2008.
- [14] Miriam Lucio Martínez. New Physics Implications And Searches At LHCb. *CERN-THESIS-2019-075*, 2019.
- [15] Wolfgang Altmannshofer, Patricia Ball, Aoife Bharucha, Andrzej J. Buras, David M. Straub, and Michael Wick. Symmetries and Asymmetries of $B \rightarrow K^* \mu^+ \mu^-$ Decays in the Standard Model and Beyond, 2008.
- [16] Wikipedia on Legendre Polynomials, https://en.wikipedia.org/wiki/Legendre_polynomials.
- [17] Tristan Arnoldus du Pree. Search for a Strange Phase in Beautiful Oscillations. *PhD Thesis*, 2010.
- [18] SymPy, <https://github.com/sympy/sympy>.

- [19] The BRUNEL project, url = <http://lhcbdoc.web.cern.ch/lhcbdoc/brunel/m>, Accessed: 07-08-2020.
- [20] StrippingBu2LLK_eeLine2, documented at:
<http://lhcbdoc.web.cern.ch/lhcbdoc/stripping/config/stripping29r2p1/leptonic> .
- [21] Wouter D. Hulsbergen. Decay chain fitting with a kalman filter. *Nuclear Instruments and Methods in Physics Research Section A: Accelerators, Spectrometers, Detectors and Associated Equipment*, 552(3):566–575, Nov 2005.
- [22] M. Pivk and F.R. Le Diberder. : A statistical tool to unfold data distributions. *Nuclear Instruments and Methods in Physics Research Section A: Accelerators, Spectrometers, Detectors and Associated Equipment*, 555(1-2):356–369, Dec 2005.
- [23] John Erthal Gaiser. Charmonium Spectroscopy From Radiative Decays of the J/ψ and ψ' . Other thesis, 8 1982.
- [24] D. Martínez Santos, P. Álvarez Cartelle, M. Borsato, V. G. Chobanova, J. García Pardiñas, M. Lucio Martínez, and M. Ramos Pernas. Ipanema: tools and examples for hep analysis on gpu, 2017.
- [25] pyCUDA, <https://pypi.org/project/pycuda/>.
- [26] iMinuit, <https://iminuit.readthedocs.io/en/stable/>.
- [27] MINUIT2, <https://root.cern.ch/doc/master/Minuit2Page.html>.
- [28] Mark Fischler and David Sachs. An object-oriented minimization package for hep, 2003.
- [29] M. Jacob and G.C. Wick. On the General Theory of Collisions for Particles with Spin. *Annals Phys.*, 7:404–428, 1959.
- [30] Frank Krüger and Joaquim Matias. Probing New Physics Via the Transverse Amplitudes of $B^0 \rightarrow K^{*0}(\rightarrow K^0 \pi^+) \ell^+ \ell^-$ at Large Recoil, 2005.